




SARS-CoV-2 Disrupts Proximal Elements in the JAK-STAT Pathway

Da-Yuan Chen,^{a,b} Nazimuddin Khan,^{a,b} Brianna J. Close,^{b,c} Raghuveera K. Goel,^{a,d} Benjamin Blum,^{a,d} Alexander H. Tavares,^{a,b} Devin Kenney,^{b,c} Hasahn L. Conway,^{a,b} Jourdan K. Ewoldt,^{e,f,g} Vipul C. Chitalia,^{h,i,j} Nicholas A. Crossland,^{b,k} Christopher S. Chen,^{e,f,g} Darrell N. Kotton,^{l,m}  Susan C. Baker,ⁿ Serge Y. Fuchs,^o  John H. Connor,^{b,c} Florian Douam,^{b,c} Andrew Emili,^{a,d}  Mohsan Saeed^{a,b}

^aDepartment of Biochemistry, Boston University School of Medicine, Boston, Massachusetts, USA

^bNational Emerging Infectious Diseases Laboratories, Boston University, Boston, Massachusetts, USA

^cDepartment of Microbiology, Boston University School of Medicine, Boston, Massachusetts, USA

^dCenter for Network Systems Biology, Boston University, Boston, Massachusetts, USA

^eDepartment of Biomedical Engineering, Boston University, Boston, Massachusetts, USA

^fBiological Design Center, Boston University, Boston, Massachusetts, USA

^gWyss Institute for Biologically Inspired Engineering, Harvard University, Boston, Massachusetts, USA

^hRenal Section, Department of Medicine, Boston University School of Medicine, Boston, Massachusetts, USA

ⁱBoston Veterans Affairs Healthcare System, Boston, Massachusetts, USA

^jInstitute of Medical Engineering and Sciences, MA Institute of Technology, Cambridge, Massachusetts, USA

^kDepartment of Pathology and Laboratory Medicine, Boston University School of Medicine, Boston, Massachusetts, USA

^lCenter for Regenerative Medicine of Boston University and Boston Medical Center, Boston, Massachusetts, USA

^mThe Pulmonary Center and Department of Medicine, Boston University School of Medicine, Boston, Massachusetts, USA

ⁿDepartment of Microbiology and Immunology, Loyola University Chicago Stritch School of Medicine, Maywood, Illinois, USA

^oDepartment of Biomedical Sciences, School of Veterinary Medicine, University of Pennsylvania, Philadelphia, Pennsylvania, USA

Nazimuddin Khan and Brianna J. Close contributed equally to this article. Author order was determined in order of increasing seniority and by mutual consent.

ABSTRACT SARS-CoV-2 can infect multiple organs, including lung, intestine, kidney, heart, liver, and brain. The molecular details of how the virus navigates through diverse cellular environments and establishes replication are poorly defined. Here, we generated a panel of phenotypically diverse, SARS-CoV-2-infectible human cell lines representing different body organs and performed longitudinal survey of cellular proteins and pathways broadly affected by the virus. This revealed universal inhibition of interferon signaling across cell types following SARS-CoV-2 infection. We performed systematic analyses of the JAK-STAT pathway in a broad range of cellular systems, including immortalized cells and primary-like cardiomyocytes, and found that SARS-CoV-2 targeted the proximal pathway components, including Janus kinase 1 (JAK1), tyrosine kinase 2 (Tyk2), and the interferon receptor subunit 1 (IFNAR1), resulting in cellular desensitization to type I IFN. Detailed mechanistic investigation of IFNAR1 showed that the protein underwent ubiquitination upon SARS-CoV-2 infection. Furthermore, chemical inhibition of JAK kinases enhanced infection of stem cell-derived cultures, indicating that the virus benefits from inhibiting the JAK-STAT pathway. These findings suggest that the suppression of interferon signaling is a mechanism widely used by the virus to evade antiviral innate immunity, and that targeting the viral mediators of immune evasion may help block virus replication in patients with COVID-19.

IMPORTANCE SARS-CoV-2 can infect various organs in the human body, but the molecular interface between the virus and these organs remains unexplored. In this study, we generated a panel of highly infectible human cell lines originating from various body organs and employed these cells to identify cellular processes commonly or distinctly disrupted by SARS-CoV-2 in different cell types. One among the

Citation Chen D-Y, Khan N, Close BJ, Goel RK, Blum B, Tavares AH, Kenney D, Conway HL, Ewoldt JK, Chitalia VC, Crossland NA, Chen CS, Kotton DN, Baker SC, Fuchs SY, Connor JH, Douam F, Emili A, Saeed M. 2021. SARS-CoV-2 disrupts proximal elements in the JAK-STAT pathway. *J Virol* 95:e00862-21. <https://doi.org/10.1128/JVI.00862-21>.

Editor Mark T. Heise, University of North Carolina at Chapel Hill

Copyright © 2021 American Society for Microbiology. All Rights Reserved.

Address correspondence to Mohsan Saeed, msaeed1@bu.edu.

Received 29 May 2021

Accepted 2 July 2021

Accepted manuscript posted online 14 July 2021

Published 9 September 2021

universally impaired processes was interferon signaling. Systematic analysis of this pathway in diverse culture systems showed that SARS-CoV-2 targets the proximal JAK-STAT pathway components, destabilizes the type I interferon receptor through ubiquitination, and consequently renders the infected cells resistant to type I interferon. These findings illuminate how SARS-CoV-2 can continue to propagate in different tissues even in the presence of a disseminated innate immune response.

KEYWORDS SARS-CoV-2, human cell lines, proteomics, virus-host interactions, IFN signaling, immune evasion, IFN antagonism, JAK-STAT pathway

SARS-CoV-2, the virus behind the ongoing COVID-19 pandemic, has claimed approximately 3.5 million human lives worldwide in a short time span of less than 18 months (1) (<https://coronavirus.jhu.edu/map.html>). The virus primarily infects lungs, causing acute respiratory distress syndrome (ARDS) and respiratory failure (2), one of the leading causes of death in COVID-19 patients. However, as more tissue specimens from infected and/or deceased individuals have become available and are probed for the presence of viral proteins or particles, there is increasing appreciation that SARS-CoV-2 can target multiple organs. Evidence for virus replication has so far been found in the intestine (3, 4), liver (5, 6), kidney (7, 8), heart (9, 10), and brain (11, 12).

The molecular mechanisms that govern the ability of SARS-CoV-2 to manipulate diverse cellular environments and navigate various body organs are unknown. One way to identify these mechanisms is to conduct a comprehensive survey of cellular pathways disrupted by the virus in distinct cell backgrounds. This, however, would require human-derived cell models that allow efficient and synchronized viral infection so as to generate a high-confidence catalog of virus-induced changes. Such systems are currently lacking, and, as a result, a large number of SARS-CoV-2 studies, including a recent genome-wide CRISPR screen to identify the viral essentiality factors (13), have been carried out in nonhuman cells.

To catalog cellular pathways broadly targeted by SARS-CoV-2, we generated a panel of six phenotypically diverse human cell lines that represented various body organs and supported high levels of SARS-CoV-2 infection. We leveraged this unique panel of cell culture models to profile proteomic responses to infection in cells originating from lung, liver, intestine, kidney, heart, and brain. This led to identification of cellular proteins and pathways widely targeted by the virus across cell types. Notable among these pathways was the JAK-STAT signaling cascade, the key component in the interferon (IFN) response pathway. Recent studies have demonstrated the inhibition of STAT phosphorylation and nuclear translocation in SARS-CoV-2-infected cells (14–16); however, the events upstream of STAT phosphorylation remain unexplored. Our molecular and functional analysis of the JAK-STAT pathway, both in cell lines and in a pluripotent stem cell-derived culture system, showed that SARS-CoV-2 disrupts the proximal signaling elements, such as IFNAR1, JAK1, and Tyk2, leading to inhibition of IFN-induced STAT phosphorylation. These results explain the mechanisms behind STAT inhibition and uncover an immune evasion strategy of SARS-CoV-2 that can be targeted for therapeutic intervention.

RESULTS

Establishing human cell lines susceptible to SARS-CoV-2 infection. Six human cell lines derived from lung, intestine, heart, kidney, liver, and brain (Fig. 1A) were infected with SARS-CoV-2 at a high multiplicity of infection (MOI) of 1 or 5, and the infection efficiency was monitored by immunofluorescence (IF) at 24 h postinfection (hpi). Three of the six cell lines, namely, A549 (lung), AC-16 (heart), and SK-N-SH (brain), were completely resistant to infection (Fig. 1B). Of the remaining three, two, Caco-2 (intestine) and HuH-6 (liver), supported low levels of SARS-CoV-2 infection (<10%), whereas HK-2 (kidney) cells were relatively more susceptible, with the number of positive cells reaching up to ~60% by 24 hpi. In contrast, around 90% of Vero cells, a

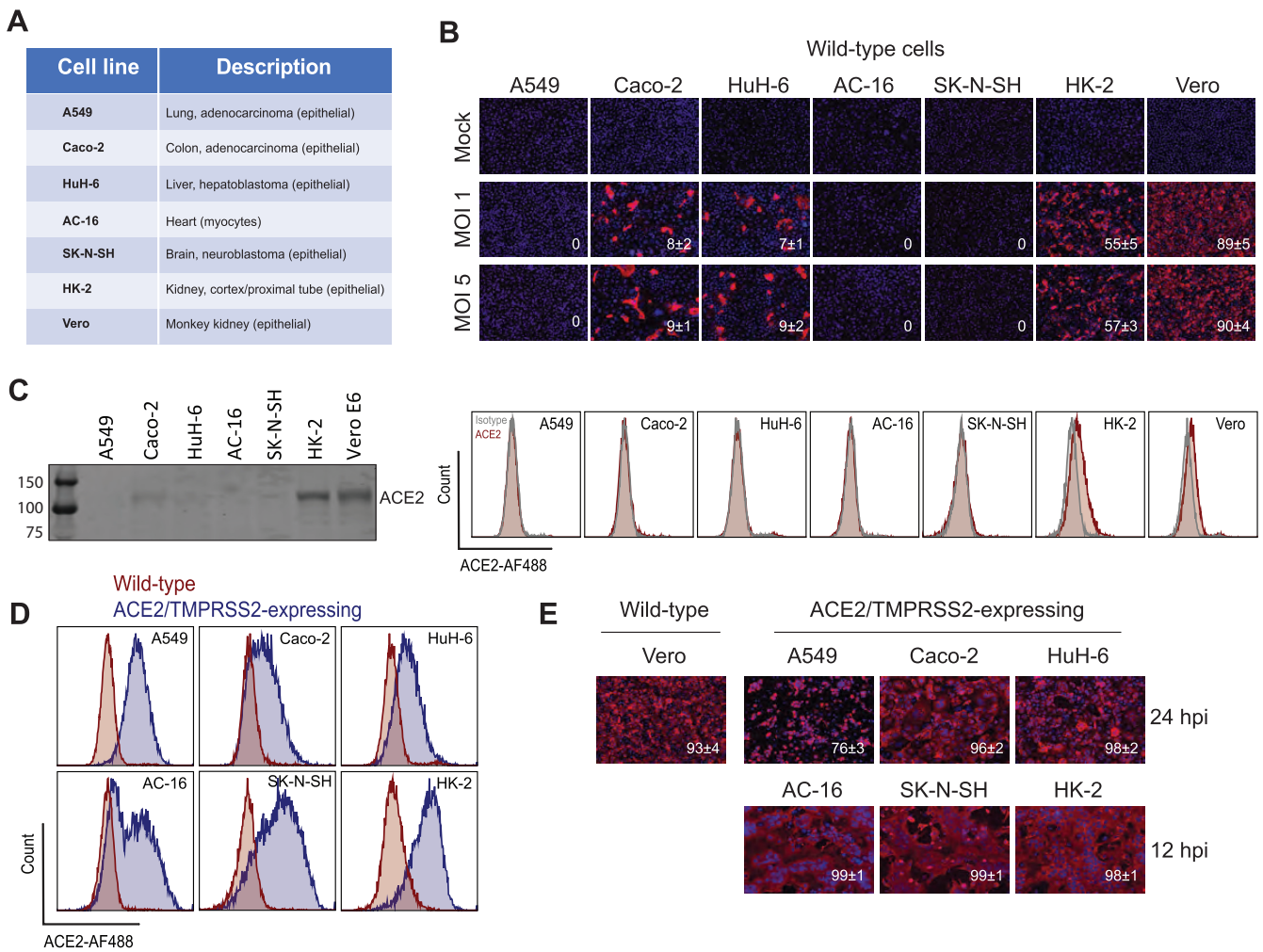


FIG 1 Susceptibility of human cells to SARS-CoV-2 infection. (A) Description of each cell line used in this study. (B) The indicated cells were infected with SARS-CoV-2 at an MOI of 1 or 5 and stained with the viral nucleocapsid (N) protein (red) at 24 hpi. The nuclei were counterstained with DAPI. The mean percentage of positive cells \pm standard deviation from three biological replicates is shown. (C) Total abundance of ACE2 in cells and its cell surface-associated fraction was measured by Western blotting (left) and flow cytometry (right), respectively. (D) Cell surface expression of ACE2 in cells transduced to express ACE2 and TMPRSS2. (E) The cells were infected with SARS-CoV-2 at an MOI of 1, followed by IF analysis of the viral N-protein (red). The nuclei were stained with DAPI. The mean percentage of positive cells \pm standard deviation from three biological replicates is shown.

monkey kidney cell line commonly used to study SARS-CoV-2 and other coronaviruses, were infected at 24 hpi.

When we analyzed ACE2 expression through Western blotting and flow cytometry (Fig. 1C), the SARS-CoV-2-susceptible cell lines HK-2 and Vero showed detectable levels of ACE2, both in lysates and on the cell surface. In Caco-2 cells, ACE2 expression was barely detectable and only by Western blotting. In contrast, HuH-6, AC-16, and SK-N-SH had no measurable levels of ACE2. Taken together, these results indicated that the cell susceptibility to SARS-CoV-2 mostly correlated with ACE2 expression. Our attempts to measure TMPRSS2, another viral entry factor, by Western blotting and flow cytometry did not yield reliable results with any of the antibodies tested (data not shown).

To investigate if exogenous expression of ACE2 and TMPRSS2 can help achieve efficient infection of the human cell lines, we generated cells stably expressing both viral entry factors. ACE2 was efficiently incorporated into the plasma membrane of all cell lines (Fig. 1D). When infected with SARS-CoV-2 at an MOI of 1, all cells, except for A549, achieved high infection levels of over 95% within 24 hpi (Fig. 1E). For A549 cells, the percentage of positive cells at 24 hpi reached only around 75%. AC-16, SK-N-SH, and HK-2 cells were almost 100% infected by 12 hpi and exhibited extensive cytopathic effects beyond this time point. Overall, these results indicate that exogenous

expression of ACE2 and TMPRSS2 was sufficient to render the human cell lines highly susceptible to SARS-CoV-2 infection.

Proteomic analysis of human cell lines infected with SARS-CoV-2. The development of human cell lines that showed uniform infection allowed us to employ global proteomic analysis to assess the impact of SARS-CoV-2 on host cells without the complication of disambiguating a mixture of uninfected and infected cells. We infected the ACE2/TMPRSS2-expressing cells with SARS-CoV-2 at an MOI of 1 and subjected them to global proteomic analysis at two different times postinfection (12 and 24 hpi for A549, Caco-2, and HuH-6; 8 and 12 hpi for AC-16, SK-N-SH, and HK-2) (Fig. 2A). To achieve a synchronized infection, we adsorbed the virus onto cells on ice for 1 h, followed by incubation at 37°C. The infections were performed in triplicate, and in-parallel analyses of time-matched, mock-infected cells were performed for comparison. Depending on the cell type, 50 to 80% cells were found infected at the first time of harvest and 80 to 100% at the second time (Fig. 2B, top two rows).

Whole proteomic analysis identified around 5,000 proteins in both uninfected and infected cells across cell lines. Despite the fact that MS²-based tandem mass tag (TMT) ratios are heavily affected by ratio compression (17), the high reproducibility among replicates allowed us to identify hundreds of differentially regulated proteins in each cell line (Fig. 2B, bottom two rows). As expected, the most highly enriched candidates in the infected cells were the viral proteins (Fig. 2C; see also File S1 in the supplemental material), including structural proteins such as spike (S), membrane (M), and nucleocapsid (N); accessory proteins such as ORF7a and ORF9b; and nonstructural components mapping to the polyprotein PP1ab (Fig. 2D), which is consistent with earlier studies (18).

Several cellular proteins were found to be differentially affected by SARS-CoV-2 in diverse or distinct cell types (File S1). We mainly focused our analysis on proteins broadly targeted by the virus across cell lines (Fig. 2E). Among such proteins were members of the ubiquitin pathway, such as USP22, UBL5, and UBE2C, which were downregulated in several cell lines. Similarly, HNRNPD (also called AUF1), a protein known to inhibit enteroviruses through degradation of the viral RNA (19), was depleted in SARS-CoV-2-infected cells. Several chemokines, which are essential mediators of inflammation and play important roles in controlling viral infections, such as CXCL1, CXCL5, CXCL8, and CXCL12, were also among the downregulated proteins. Consistent with previous reports, several proteins involved in cell cycle regulation, including TOB2, AURKA, and AURKB, were diminished upon SARS-CoV-2 infection (20). We also identified differential regulation of several innate immune components in the proteomic data set. For instance, JAK1 and SERPINE1 were downregulated, whereas IFI35, which has been shown to negatively regulate antiviral responses, was enriched following SARS-CoV-2 infection (Fig. 2E).

We performed Western blot analysis on a subset of proteins that showed differential regulation in our proteomics analysis. As controls, we included two additional viruses, yellow fever virus (YFV) and coxsackievirus B3 (CVB3), to rule out any general stress responses induced upon a positive-sense RNA virus infection (Fig. 3A). Western blotting largely revealed protein expression patterns consistent with the proteomics results (Fig. 3B and C). As an example, USP22 was depleted in all cell lines tested, while APOE was impaired in a small subset of cells. For the most part, YFV and CVB3 infection did not affect the selected proteins, with the exception of TOB2, which was depleted in all virus-infected cells. It should be noted that, like SARS-CoV-2, CVB3 is known to quickly shut down host translation and promote protein degradation (21), yet CVB3 did not suppress the expression of most of the proteins inhibited by SARS-CoV-2, suggesting that the decreased protein levels in SARS-CoV-2-infected cells were not a reflection of generalized perturbation of proteostasis. Overall, these results confirmed the authenticity of our proteomic data set and indicate that most of the alterations we detected in the infected cells were specifically due to SARS-CoV-2 infection rather than simply a generic response to viral invasion.

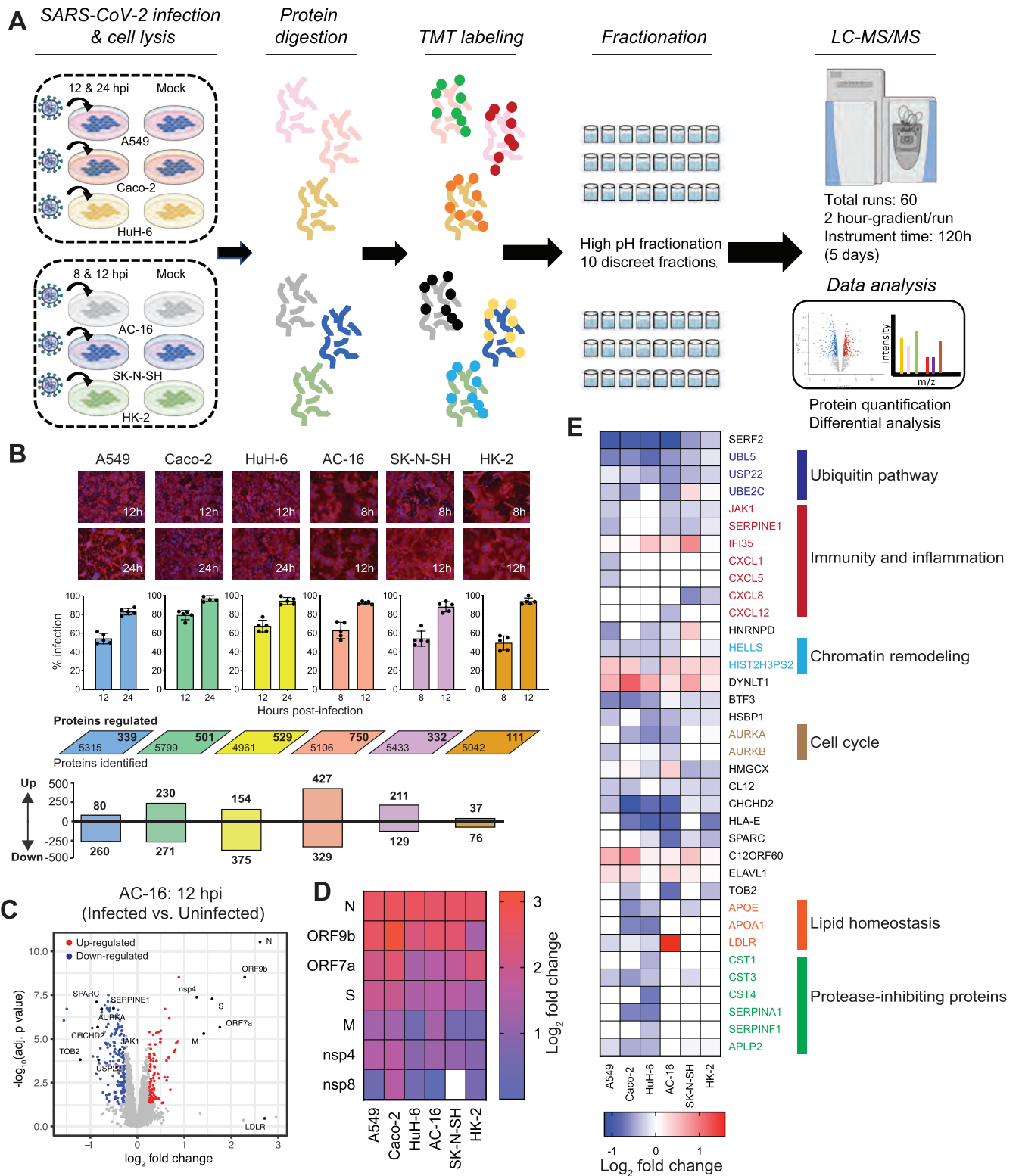


FIG 2 Global proteomic analysis of SARS-CoV-2-infected cells. (A) Schematics of the proteomics pipeline. Total protein was extracted from the SARS-CoV-2-infected and uninfected cells, trypsinized, and isotope (TMT) labeled. The peptides for each cell line were separately pooled, fractionated, sequenced, and quantified by liquid chromatography-tandem mass spectrometry (LC-MS/MS). (B) The cells were infected with SARS-CoV-2 at an MOI of 1 and processed at 12 and 24 hpi (A549, Caco-2, and HuH-6) or at 8 and 12 hpi (AC-16 and SK-N-SH) for IF and proteomic analysis. The top panel shows the IF images (red color, viral N protein; blue color, DAPI). The percentage of positive cells was measured and plotted as the mean \pm standard deviation from five microscopic fields. The rhomboids show the total number of proteins identified in uninfected and infected cells (lower left corner) as well as the total number of regulated proteins in each cell line across both time points following SARS-CoV-2 infection (upper right corner). Numbers of distinct proteins (Continued on next page)

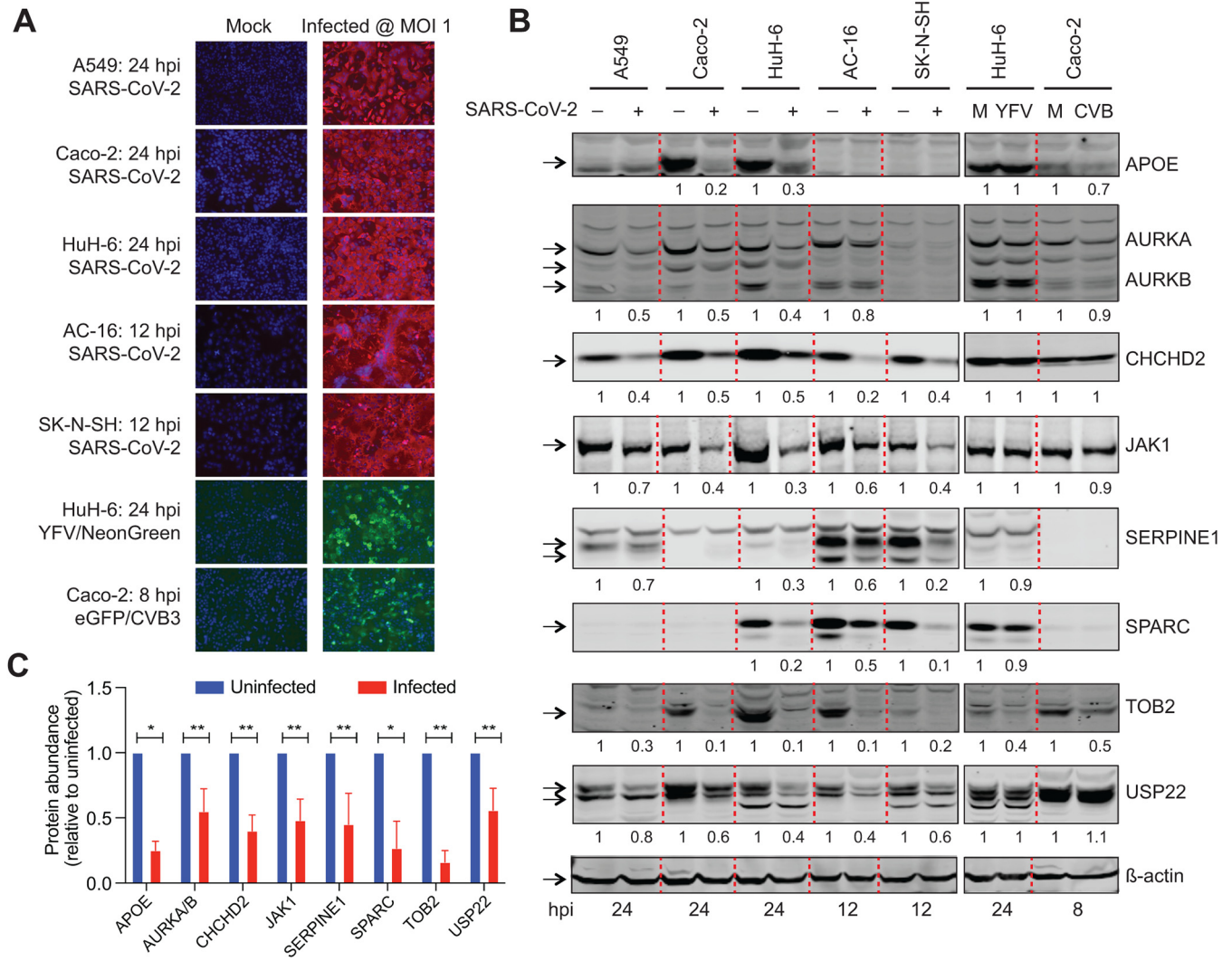


FIG 3 Validation of proteomic results by Western blotting. (A) ACE2/TMPRSS2-expressing A549, Caco-2, HuH-6, AC-16, and SK-N-SH cells were infected with freshly prepared SARS-CoV-2. As a control, Huh-6 cells were infected with YFV 17D virus containing the NeonGreen reporter (MOI of 1) and Caco-2 cells with CVB3 containing the GFP reporter. The cells were fixed at the indicated times and processed for IF and/or imaging. (B) The cells were lysed in RIPA buffer followed by Western blot analysis of the indicated proteins. An equal amount of total protein (25 μ g), as quantified by the BCA assay, was loaded in each lane. The black arrows indicate the protein bands of expected sizes. M, mock. The numbers indicate band intensities, with the uninfected cell values arbitrarily set at 1. The experiment was done only once; however, different cell lines were infected at different times to ensure the rigor and reproducibility of our results. (C) The SARS-CoV-2 numbers from panel B were pooled and plotted as a graph. *, *P* value between 0.01 and 0.05; **, *P* \leq 0.01, as calculated by a two-tailed, unpaired *t* test with Welch's correction.

SARS-CoV-2 downregulates proximal elements in the JAK-STAT pathway. Recent studies have demonstrated the ability of SARS-CoV-2 to inhibit IFN-mediated STAT phosphorylation and nuclear translocation (14, 15); however, the events upstream of STAT phosphorylation are unclear. Our proteomic analysis of SARS-CoV-2-infected cells and subsequent validation of select hits revealed universal downregulation of JAK1 (Fig. 3B and C), a key signaling protein operating upstream of STATs and downstream of IFN and other cytokines, such as interleukin-2 (IL-2), IL-4, IL-6, and IL-7 (22, 23). This prompted us to probe the

FIG 2 Legend (Continued)

up- or downregulated after infection are shown in the bottom panel. In certain cases, the total numbers of up- and downregulated proteins do not match the numbers shown in rhomboids. This is due to some proteins downregulated at one time point and upregulated at the other time point. (C) Volcano plot of proteins regulated in AC-16 cells upon SARS-CoV-2 infection. Proteins enriched in infected cells are shown in red, while those depleted are in blue. Black color is used for the proteins labeled with their names. (D) Heat map showing the abundance of viral proteins in different cell lines. (E) Heatmap visualization of cellular proteins found to be differentially regulated in more than one cell line. The pathways to which some of these proteins belong are shown on the right.

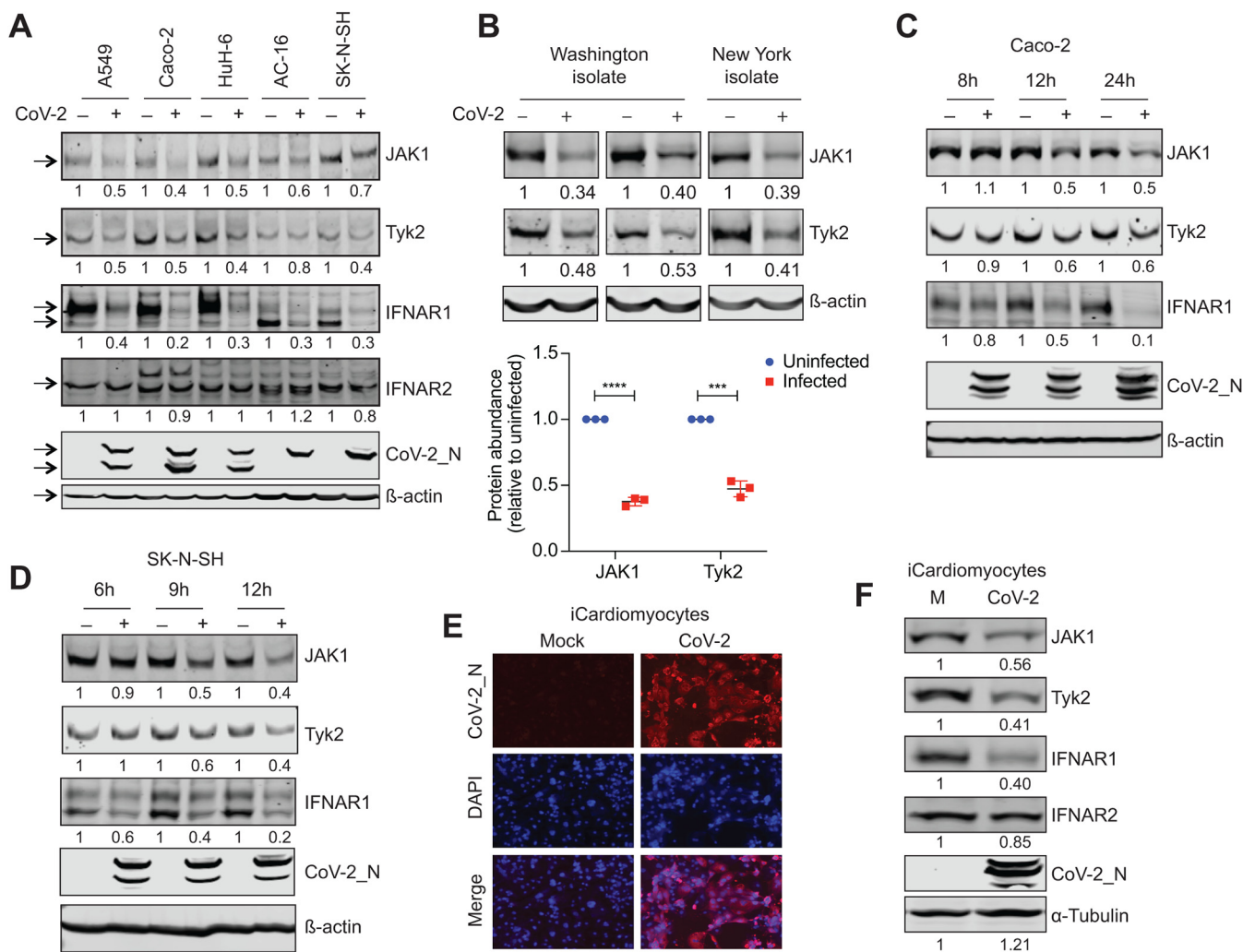


FIG 4 SARS-CoV-2 disrupted the expression of IFNAR1 and JAK proteins. All cells used in this figure were engineered to overexpress ACE2 and TMPRSS2. (A) A549, Caco-2, and HuH-6 cells were infected with SARS-CoV-2 at an MOI of 1 for 24 h and AC-16 and SK-N-SH for 12 h, followed by Western blotting. The numbers indicate band intensities, with the uninfected cell values arbitrarily set at 1. The black arrows indicate the protein bands of expected sizes. The experiment was performed once; however, different cell lines were infected at different times to ensure reproducibility of our results. (B) Caco-2 cells were infected with either the Washington isolate (two replicates) or the New York isolate (one replicate) of SARS-CoV-2 (MOI of 1) for 24 h, and the expression of JAK1, Tyk2, and β -actin was analyzed by Western blotting. The band intensities relative to uninfected cells are shown. The numbers from these independently performed Western blots, representing three biological replicates (two with the Washington isolate and one with a New York isolate), were pooled and plotted as a graph in the bottom panel. ****, $P=0.0009$; ***, $P=0.004$; calculated by a two-tailed, unpaired t test with Welch's correction. (C and D) Caco-2 (C) and SK-N-SH (D) cells were infected with SARS-CoV-2 at an MOI of 1, followed by detection of the indicated proteins by Western blotting. The band intensities relative to uninfected cells are shown. Representative images from two experimental repeats are shown. (E and F) hiPSC-CMs were infected with SARS-CoV-2 at an MOI of 5 (calculated based on virus titration in Vero E6 cells) for 72 h, followed by IF (E) and Western blotting (F). The relative band intensities are shown. The experiment was only performed once.

role of JAK1 and other proximal elements in the JAK-STAT pathway, such as tyrosine kinase 2 (Tyk2) and the IFN- α receptor (IFNAR), in SARS-CoV-2-mediated inhibition of STAT phosphorylation. We found that, like JAK1, the expression of Tyk2 was also downregulated in most of the cell lines tested (Fig. 4A). We confirmed the depletion of JAK1 and Tyk2 in Caco-2 cells infected with two different SARS-CoV-2 isolates at an MOI of 1 (Fig. 4B). When we tested the abundance of IFNAR, we found strong inhibition of IFNAR1, but not IFNAR2, following SARS-CoV-2 infection (Fig. 4A). Detailed time course investigation showed that most of the JAK-STAT components were depleted early in infection (Fig. 4C and D), when the cytopathic effect of virus was not apparent (data not shown), indicating a quick active repression of protein abundance as opposed to collateral effects of generalized gene inhibition often observed late during infection.

To confirm the authenticity of these findings in a more physiologically relevant

setting, we established a human induced pluripotent stem cell (hiPSC)-derived model of SARS-CoV-2 infection and monitored the ability of the virus to impair IFN-related proteins. We differentiated hiPSC into cardiomyocytes (hiPSC-CM) and first assessed their ability to support virus infection. IF analysis showed that these cells were highly permissive to SARS-CoV-2 infection, and when infected at an MOI of 5 (based on virus titration performed in Vero cells), most of the cells became positive by 72 hpi (Fig. 4E). In these infected cardiomyocytes, we observed strong depletion of JAK1, Tyk2, and IFNAR1 but not of IFNAR2, consistent with the cell line data (Fig. 4F). These results clearly indicate that SARS-CoV-2 causes bona-fide inhibition of proximal elements in the interferon response pathway.

SARS-CoV-2-infected cells are resistant to type I interferon and IL-6. Engagement of IFN to its receptor complex and the subsequent activation of receptor-associated JAK kinases leads to tyrosine phosphorylation, dimerization, and activation of STAT proteins (24). Because SARS-CoV-2 inhibited the expression of IFN receptor and its associated JAKs, we next determined if this inhibition desensitized the infected cells to IFN treatment. For this, we treated uninfected and infected cells with IFN- α and examined the phosphorylation of three main STATs involved in IFN signaling, namely, STAT1, STAT2, and STAT3. As expected, IFN treatment of uninfected cells for 30 min caused extensive phosphorylation of all three STATs without influencing the abundance of total proteins (Fig. 5A). In contrast, however, the virus-infected cells were highly resistant to IFN- α , with STAT phosphorylation being reduced by over 90% compared to uninfected cells. Interestingly, the abundance of total STAT2 protein was also diminished in infected cells, indicating an additional layer of virus-imposed inhibition of IFN signaling. To further confirm these findings, we performed a dose-response analysis of STAT phosphorylation upon IFN treatment. While escalating doses of IFN caused increasing phosphorylation of STATs in uninfected cells, only a negligible effect was seen in SARS-CoV-2-infected cells (Fig. 5B). This refractoriness to exogenous IFN can stem from the action of endogenous IFN produced in response to virus infection. However, Vero E6 cells, which lack the ability to produce endogenous IFN (25), were also highly resistant to IFN- α treatment following SARS-CoV-2 infection (Fig. 5C), suggesting that the endogenously produced IFN was not responsible for the observed phenotype. Furthermore, consistent with the results obtained from human cell lines, Vero E6 cells also exhibited IFNAR1 depletion following SARS-CoV-2 infection. Finally, SARS-CoV-2-infected cells exhibited strong desensitization to IL-6, a proinflammatory cytokine that also signals through JAK proteins (26) (Fig. 5D and E).

Once activated by phosphorylation, STAT proteins make homo- or heterodimers and translocate to the nucleus, where they activate the expression of interferon-stimulated genes (ISGs) (24). Consistent with the decreased phosphorylation of STAT proteins following SARS-CoV-2 infection, we observed strong inhibition of STAT1 nuclear translocation. While most of the STAT1 protein in uninfected cells moved to the nucleus within 30 min of IFN treatment, it largely remained in the cytoplasm in SARS-CoV-2-infected cells (Fig. 5F). This was associated with a significant loss of ISG induction. We treated uninfected and virus-infected cells with IFN for 1, 2, 4, and 8 h and examined the expression of three ISGs, ISG15, IFIT1, and RSAD2 (also called Viperin), by quantitative real-time PCR (RT-qPCR). Remarkably, while IFN caused 3- to 85-fold up-regulation of ISGs in uninfected cells, the expression levels remained unchanged in the infected cell (Fig. 5G and File S1). We note that the cytoplasmic retention of STAT1 and subsequent inhibition of ISG induction in SARS-CoV-2-infected cells cannot be solely attributed to the dysregulation of proximal JAK-STAT components, because SARS-CoV-2 also employs other means to perturb STAT1 nuclear translocation, including disruption of Karyopherin cargo receptors (14, 16). In all, these results indicate that SARS-CoV-2 transforms infected cells into an interferon nonresponsive state.

SARS-CoV-2 induces IFNAR1 ubiquitination and inhibits IFN-mediated phosphorylation of JAK1 and Tyk2. While protein expression of IFNAR1 was severely impaired in SARS-CoV-2-infected cells, the mRNA levels remained unchanged (Fig. 6A), suggesting that the regulation mainly occurred at the posttranscriptional stage. Therefore, to

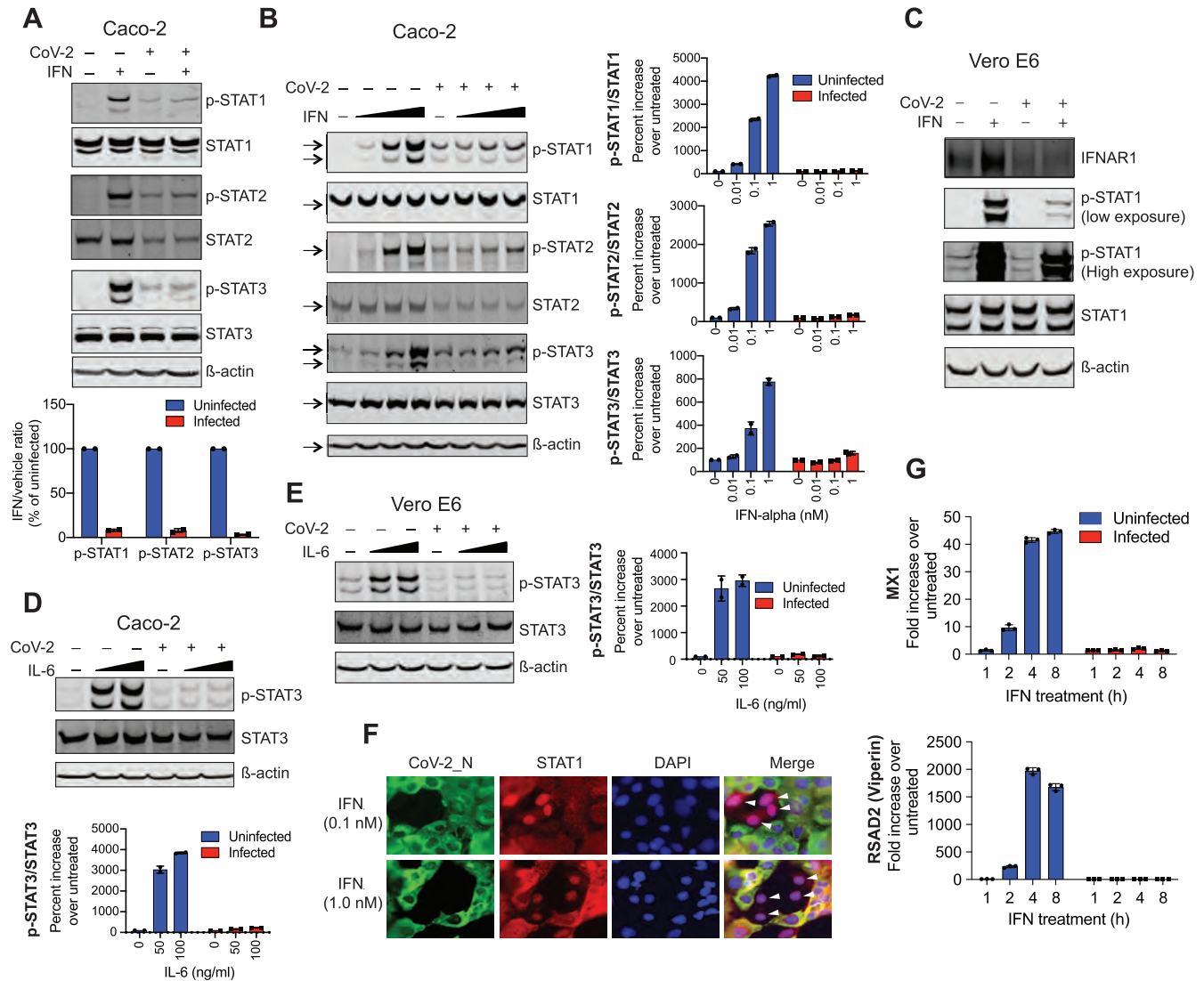


FIG 5 SARS-CoV-2 inhibited IFN signaling. (A) Uninfected Caco-2 cells or the ones infected with SARS-CoV-2 (MOI of 1) for 24 h were treated with human IFN- α (1 nM) or, as a negative control, with vehicle (PBS) for 30 min, followed by Western blotting. The band intensities of the phospho-STATs were normalized against the total STATs and plotted in the bottom panel as a percentage of uninfected cells. The data are presented as mean \pm standard deviation from two experimental repeats. (B) Uninfected or SARS-CoV-2-infected Caco-2 cells (24 hpi) were treated with 0, 0.01, 0.1, or 1 nM IFN- α for 30 min and subjected to Western blotting. The band intensities for two experimental repeats are presented as mean \pm standard deviation on the right. The intensities for untreated cells were set at 100, and the percent increase in IFN-treated cells was measured by calculating the ratio between IFN-treated and untreated cells. (C) Uninfected or SARS-CoV-2-infected Vero E6 cells were treated with 1 nM IFN- α for 30 min and subjected to Western blotting. (D and E) Uninfected or SARS-CoV-2-infected Caco-2 or Vero E6 cells (24 hpi) were treated with 0, 50, or 100 ng/ml IL-6 for 30 min and subjected to Western blotting. The graphs show the mean \pm standard deviation band intensities from two experimental repeats. (F) Caco-2 cells infected with SARS-CoV-2 for 24 h were exposed to 0.1 or 1 nM IFN- α for 30 min and stained for the viral N protein (green) and STAT1 (red). The nuclei were stained with DAPI (blue). The nuclear translocation of STAT1 is indicated with white arrowheads. (G) Caco-2 cells, uninfected or infected with SARS-CoV-2 for 24 h, were treated with IFN (1 nM) for 1, 2, 4, or 8 h, and RNA levels of MX1 and Viperin (also called RSAD2) were measured by RT-qPCR. RPS11 served as a housekeeping gene. The data are plotted as mean \pm standard deviation from three biological replicates.

examine the molecular basis of IFNAR1 downregulation, we analyzed the extent of IFNAR1 ubiquitination in the infected cells. For this, we transfected cells with FLAG-IFNAR1 and hemagglutinin (HA)-ubiquitin, infected them with SARS-CoV-2 at different multiplicities of infection, and analyzed IFNAR1 ubiquitination. A remarkable increase in protein ubiquitination was seen in the infected cells (Fig. 6B), to levels almost similar to those in cells treated with thapsigargin, a known inducer of IFNAR1 ubiquitination (27). To confirm if endogenous IFNAR1 also undergoes ubiquitination upon SARS-CoV-2 infection, we employed a trypsin-resistant tandem ubiquitin-binding entity (TR-TUBE), which directly binds polyubiquitin chains and protects them from degradation (28). We included vesicular stomatitis

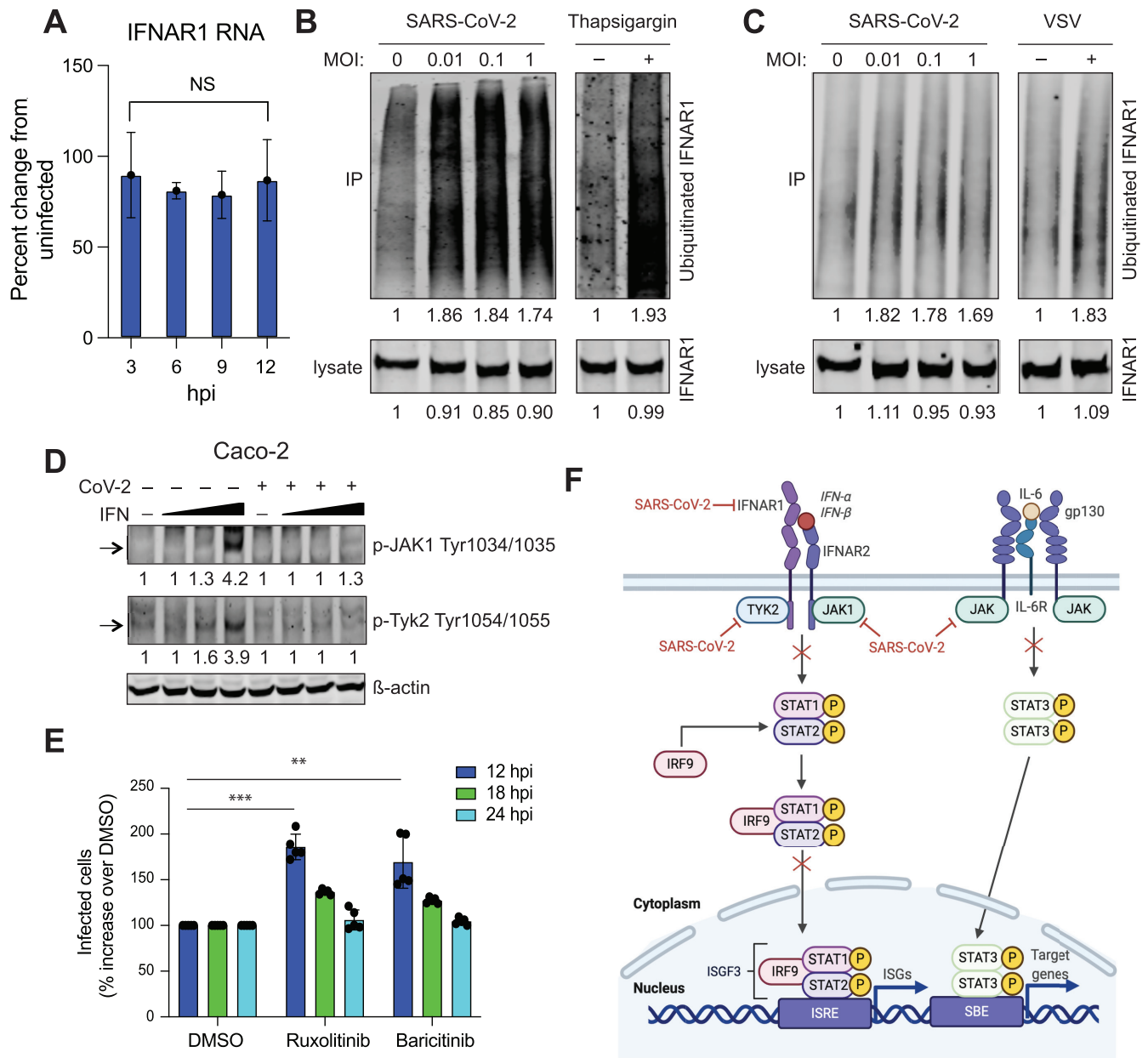


FIG 6 SARS-CoV-2 destabilized the IFNAR1 protein. (A) mRNA levels of IFNAR1 were analyzed by RT-qPCR in Caco-2 cells infected with SARS-CoV-2 for the indicated times. RPS11 mRNA levels were used for data normalization. The data are plotted as mean \pm standard deviation from three biological replicates. NS, nonsignificant, as calculated by a two-tailed, unpaired *t* test with Welch's correction. (B) Ubiquitination of ectopically expressed IFNAR1 was examined in 293T/ACE2/TMPRSS2 cells infected with SARS-CoV-2. Thapsigargin treatment served as a positive control. The numbers indicate band intensities, with the uninfected cell numbers arbitrarily set at 1. (C) Ubiquitination of endogenous IFNAR1 following SARS-CoV-2 infection, as assessed by the binding of TR-TUBE to the IFNAR1 protein. Cells infected with VSV were included as a positive control. A representative image from one of the two experimental repeats is shown. The numbers indicate band intensities, with the uninfected cell numbers arbitrarily set at 1. (D) Uninfected or SARS-CoV-2-infected Caco-2 cells (24 hpi) were treated with 0, 0.01, 0.1, or 1 nM IFN- α for 20 min and subjected to Western blotting with antibodies specific for the indicated phosphoforms of JAK1 and Tyk2. (E) hiPSC-CMs were infected with SARS-CoV-2 at an MOI of 5 in the presence of DMSO or 5 μ M compounds. IF was performed at 12, 18, and 24 hpi, and the number of positive cells was counted by Muvicyte (see Materials and Methods). The data are plotted as mean \pm standard deviation from five biological replicates from two experimental repeats. **, *P* = 0.006; ***, *P* = 0.0002; calculated by a two-tailed, unpaired *t* test with Welch's correction. (F) Model of the JAK-STAT inhibition by SARS-CoV-2. Proteins and signaling steps disrupted by the virus are indicated with red inhibition arcs.

virus (VSV) as a control, because infection with VSV has previously been shown to cause ubiquitination of endogenous IFNAR1 (27). After immunoprecipitation of TR-TUBE, high-molecular-weight ubiquitinated species of IFNAR1 were found to be more abundant in lysates of cells infected with both SARS-CoV-2 and VSV compared to uninfected cells (Fig. 6C), strengthening our conclusion that SARS-CoV-2 destabilizes IFNAR1 through

ubiquitination. In agreement with the ability of TR-TUBE to prevent protein degradation (29), no decrease in IFNAR1 levels was observed in the lysates of TR-TUBE-transfected cells following infection (Fig. 6C, bottom). As expected from IFNAR1 downregulation, type I IFN failed to induce phosphorylation of JAK1 and Tyk2 in virus-infected cells (Fig. 6D), although this perturbation was confounded by the lower steady-state levels of JAK proteins in the infected cells (Fig. 4A to D). Finally, chemical inhibition of JAKs with inhibitors ruxolitinib and baricitinib, which are known to inhibit cell responsiveness to IFN (30, 31), increased SARS-CoV-2 infection of hiPSC-CMs, as evidenced by a 1.5- to 2-fold increase in the percentage of virus-infected cells at 12 hpi, although this replicative advantage was lost by 24 hpi (Fig. 6E). In total, these results indicate that SARS-CoV-2 desensitizes the infected cells to type I IFN through inhibition of proximal elements in the JAK-STAT pathway (Fig. 6F).

DISCUSSION

We report that SARS-CoV-2 disrupts the proximal JAK-STAT pathway components, limiting IFN signaling and facilitating virus replication in diverse tissue types. Being among the earliest and most potent of the immune responses, IFN signaling poses an immediate threat to viruses and can quickly eliminate them from the infected cells. Two recent reports have shown that inborn errors in IFN signaling and the presence of anti-IFN autoantibodies can predispose individuals to a life-threatening COVID-19 disease, highlighting the importance of IFN immunity in SARS-CoV-2 infection (32, 33). Our findings complement these reports and show that SARS-CoV-2 has evolved a suite of mechanisms to counteract the effector functions of interferon. This inhibition of IFN signaling is also expected to attenuate the production of IFN, as these two processes are tightly regulated by a positive feedback loop, with early IFNs inducing the expression of viral sensors (34), interferon regulatory factor 7 (IRF7), and other signaling molecules (35), which regulate the expression of IFN (36). The overall outcome of this inhibition is an attenuated antiviral state supporting uninterrupted viral propagation in disparate tissues.

Recent studies have described the inhibition of the JAK-STAT pathway by SARS-CoV-2 and its encoded proteins (14, 15). The ORF6 protein of SARS-CoV-2 was shown to inhibit the nuclear translocation of STAT in response to IFN (16). Our study expands the repertoire of possible mechanisms and shows that SARS-CoV-2 impairs proximal JAK-STAT components acting upstream of STAT activation and nuclear translocation. Interestingly, we also noticed a depletion of STAT2 in SARS-CoV-2 infected cells. While STAT1 and STAT2 have comparable half-lives (37), the fact that only STAT2 levels were diminished following SARS-CoV-2 infection suggests that the virus represses specific proteins as opposed to a general inhibition of protein expression. The infection strongly affected IFNAR1 expression, causing 60 to 90% depletion of this protein (Fig. 4A, C, D, and F). The JAK kinases, associated with the cytoplasmic side of IFN receptors and involved in intracellular signal transduction, were also diminished. Because Tyk2 physically interacts with IFNAR1 (38) (Fig. 6F), the decrease in Tyk2 levels can be explained by IFNAR1 degradation. However, the processes governing the inhibition of JAK1, an interacting partner of IFNAR2, are unclear and could very well be completely different from those operating on Tyk2. A detailed mechanistic analysis is required to dissect the inhibition of proximal JAK-STAT components in SARS-CoV-2-infected cells and will be the focus of our future investigations.

SARS-CoV-2 infection induced a small degree of STAT phosphorylation in Caco-2 cells (Fig. 5A and B), suggesting that these cells inherently produce IFN and/or other cytokines in response to virus infection, which then bind to their cognate receptors and initiate signal transduction. This raises the possibility that the resistance of SARS-CoV-2-infected cells to exogenous IFN simply reflects the state of refractoriness created by the action of endogenous IFN (39). However, Vero E6 cells, which lack the ability to produce endogenous IFN due to spontaneous gene deletions (25), also exhibited lower responsiveness to exogenous IFN (Fig. 5C), indicating that SARS-CoV-2-mediated desensitization of host cells to exogenous IFN is independent of the production and

activity of endogenous IFN. While SARS-CoV-2 uses the endosomal route to gain entry into Vero E6 cells (40), its invasion of A549/ACE2/TMPRSS2 appears to be mediated through TMPRSS2 (41); however, since both cell lines lost responsiveness to type I IFN following SARS-CoV-2 infection (Fig. 5C; data not shown for A549), the route of viral entry does not seem to be a determining factor for resistance to IFN.

Several studies are currently evaluating the clinical efficacy of IFN alone or in combination with antiviral compounds for the treatment of COVID-19 (<https://clinicaltrials.gov>). This is based on the supposition that IFNs can help clear infection in two ways, first by acting on infected cells and eliminating the replicating virus and, second, by creating an antiviral state in uninfected cells to block viral spread. There is support for the latter mechanism of action from recent studies showing that pretreatment with IFN can effectively inhibit SARS-CoV-2 replication in cell culture (42, 43). However, our results show that once the viral replication is established inside a cell, its ability to respond to IFN is severely compromised, suggesting that the former potential protective mechanism of IFN treatment does not function in COVID-19 patients. In a clinical setting, by the time a patient receives IFN treatment, a large number of cells are infected with the virus, and these would be expected to be nonresponsive to interferon treatment. This notion is further supported by a recent finding that despite high levels of IFN produced by primary human airway epithelial cells during SARS-CoV-2 infection, this IFN was unable to control viral replication (44).

Considering this scenario, the timing of IFN therapy relative to infection is expected to be the key determinant of outcome. In a recent retrospective study of 446 patients with COVID-19, early use of IFN was found to be protective, whereas its late administration was associated with delayed recovery and increased mortality (45). Similarly, the World Health Organization's large-scale, multicountry clinical trial showed no protective effect of IFN in hospitalized COVID-19 patients with late-stage disease (<https://www.medrxiv.org/content/10.1101/2020.10.15.20209817>). The same has been previously reported in mice infected with a related human coronavirus, Middle East respiratory syndrome-CoV, where early administration of IFN protected the animals from lethal infection, whereas delayed administration of IFN failed to inhibit virus replication (46). This limited efficacy of IFN at later stages of infection can also be explained by several other factors, such as the route of IFN administration, use of IFN as a combination therapy with immunosuppressive drugs (i.e., corticosteroids), and the type of IFN being used.

Of note, the activation of the JAK-STAT pathway has been shown to stimulate the production of IL-6 and other inflammatory cytokines (47), which in turn attract an army of immune cells to the site of infection to orchestrate the destruction of infected cells. Therefore, inhibition of the JAK-STAT axis by SARS-CoV-2 can suppress the production of cytokines, thereby disrupting a potent and timely inflammatory response. The interferon pathway is also implicated in cross talk between innate and adaptive immunity (48). Loss of bridging between these two immunity arms and the resulting timing mismatch has been postulated to cause severe disease in COVID-19 patients (49, 50). A recent study that examined peripheral blood from patients with COVID-19 of various severities also reported a strong correlation between impairment of IFN responses and the clinical outcome of infection (51). These two observations, when combined, firmly point to the possibility of aberrant IFN responses at the heart of COVID-19 pathogenesis.

Interestingly, we found that JAK inhibitors ruxolitinib and baricitinib enhanced SARS-CoV-2 infection in stem cell-derived cardiomyocytes, which is consistent with a recent report showing a significant increase in viral infection following baricitinib treatment of cultured cells (52). However, baricitinib has been approved by the U.S. Food and Drug Administration (FDA) as part of a combination therapy with remdesivir to be used under an Emergency Use Authorization (EUA) in hospitalized patients with severe COVID-19 disease (53). Although the mechanism by which baricitinib helps these patients is not entirely clear, it is believed to act by inhibiting the intracellular signaling cascades initiated by cytokines known to be aberrantly elevated in severe COVID-19.

Given the replication-enhancing effect of baricitinib at earlier stages of infection, its clinical potential should be more carefully investigated.

Our study reports a suite of human cell lines suitable for SARS-CoV-2 studies. Exogenous expression of ACE2 has been demonstrated to improve the susceptibility of a few human cell lines, such as A549 and HeLa, to SARS-CoV-2 (54, 55), but our results show that efficient infection can only be achieved when ACE2 and TMPRSS2 are coexpressed. This finding is important, because it provides a conceptual framework for generating efficient infection models for SARS-CoV-2. Human ACE2-expressing mice that are currently used to investigate SARS-CoV-2 (56) do not recapitulate the full spectrum of the human disease (reviewed in reference 57). From our results, it is tempting to speculate that coexpression of human ACE2 and TMPRSS2 will improve the quality and physiological relevance of these mouse models.

The human cell lines we generated represent a rich resource that can be used to investigate cellular pathways broadly targeted by SARS-CoV-2 in diverse tissue types. While immortalized and cancerous cell lines often incompletely recapitulate the genotypic and phenotypic profile of their tissues of origin, many cell lines maintain an important degree of tissue identity (58). This is reflected in our proteomic data set. As an example, APOE, a protein regulated upon virus infection and which we validated by Western blotting, was only found to be altered in liver and intestinal cell lines, two tissue types known to express this protein to high levels (59). The results obtained from hiPSC-CMs closely matched those from the cardiac cell line AC-16, providing further validity to our cell line approach (Fig. 4A and F).

Recent studies have reported proteomic profiling of SARS-CoV-2 infection in Caco-2 (18) and A549 (52) cells. These studies, however, employed relatively suboptimal infection models and, thus, relied on a mosaic of infected and uninfected cells. We found little overlap between our results and those reported by others. This could be due to the differences in viral isolates, proteomic platforms, and analyses pipelines but is likely also due to disparities in the number of infected cells in the cell population. Our infection models supported quick, uniform virus infection, allowing us to identify SARS-CoV-2-specific changes as opposed to generalized stress responses, as evident from the Western blot analysis of select hits in cells infected with two noncoronaviruses (Fig. 3B).

In all, this study reveals SARS-CoV-2-mediated desensitization to IFN in multiple cell types and identifies the proximal JAK-STAT components as a target of viral antagonism. These findings enhance our understanding of how SARS-CoV-2 mutes the innate immune system to sustain its replication, leading to impaired adaptive immune responses and, consequently, severe disease. The knowledge gained from these studies will provide the foundation for the development of therapeutic interventions aimed at boosting cell-intrinsic antiviral responses and inform the design of attenuated viruses as potential vaccine candidates.

MATERIALS AND METHODS

Cells, antibodies, and chemicals. All cell lines were incubated at 37°C and 5% CO₂ in a humidified incubator. Human embryonic kidney HEK293T cells (ATCC; CRL-3216), human lung adenocarcinoma A549 cells (ATCC; CCL-185), human hepatoblastoma HuH-6 cells (JCRB-0401), human kidney papilloma HK-2 cells (ATCC; CRL-2190), human neuroblastoma SK-N-SH cells (ATCC; HTB-11), and African green monkey kidney Vero E6 cells were maintained in Dulbecco's modified Eagle medium (DMEM) (number 11995-065; Gibco) containing 10% fetal bovine serum (FBS) and 1× nonessential amino acids. Human colorectal adenocarcinoma Caco-2 cells (HTB-37; ATCC) were maintained in the same medium but containing 20% FBS, whereas human cardiomyocyte AC16 cells (SCC109; Millipore) were cultured in DMEM/F12 (number 11330-032; Gibco) containing 12.5% FBS. Mycoplasma-negative status of all cell lines was confirmed. Cells stably expressing human ACE2 and TMPRSS2 were generated by lentiviral transduction followed by selection with appropriate selection drugs.

Anti-SARS-CoV nucleocapsid (N) protein antibody (number 200-401-A50; Rockland) was used for detection of SARS-CoV-2 N protein by IF. Anti-hACE2 antibodies included rabbit monoclonal antibody EPR4435 (2) (number ab108252; Abcam) for Western blotting and goat polyclonal antibody (number AF933; R&D Systems) for flow cytometry. Goat IgG isotype control antibody was from Invitrogen (number 02-6202). Antibodies for validation of our proteomics results and the follow-up studies included APOE (number 18254-1-AP; Proteintech), AURKA (number A300-071A; Bethyl Laboratories), CHCHD2 (number 19424-1-AP; Proteintech), JAK1 (number 3344; Cell Signaling Technologies), p-JAK1 (number 74129; Cell Signaling

Technologies), LDLR (number A304-417A; Bethyl Laboratories), SERPINE1 (NBP1-19773; Novus Biologicals), SPARC (number 15274-1-AP; Proteintech), TOB2 (number 13607-1-AP; Proteintech), USP22 (number NBP1-49644; Novus Biologicals), Tyk2 (number 67411-1-Ig; Proteintech), p-Tyk2 (number 9321; Cell Signaling Technologies), p-STAT1 (number 9171; Cell Signaling Technologies), STAT1 (number 14994; Cell Signaling Technologies), pSTAT-2 (number 4441; Cell Signaling Technologies), STAT2 (number sc-476; Santa Cruz Biotechnology), pSTAT3 (number 9145; Cell Signaling Technologies), STAT3 (number sc-482; Santa Cruz Biotechnology), β -actin (number AM4302; Invitrogen), and α -tubulin (number TM4111; ECM Biosciences).

Ruxolotinib (INCB018424) was from Selleck Chemicals (number S1378), and baricitinib phosphate was from Fisher Scientific (number 50-201-3519).

Plasmids. The plasmids pCAGGS_TMPRSS2-Flag and pcDNA3.1_ACE2, encoding human ACE2 and TMPRSS2, respectively, were obtained from Thomas Gallagher (Loyola University). We transferred ACE2 and untagged TMPRSS2 to the lentiviral pLOC vector to obtain pLOC_hACE2_PuroR and pLOC_hTMPRSS2_BlastR, respectively.

SARS-CoV-2 stock preparation and titration. We used the 2019-nCoV/USA-WA1/2020 isolate (NCBI accession number [MN985325](#)) of SARS-CoV-2, obtained from the Centers for Disease Control and Prevention and BEI Resources. To generate the passage 1 (P1) virus stock, we infected Vero E6 cells, seeded 1 day prior into a 175-cm² flask at a density of 10 million cells, with the master stock diluted in 10 ml of Opti-MEM. Following virus adsorption to the cells at 37°C for 1 h, we added 15 ml of DMEM containing 10% FBS and 1× penicillin-streptomycin. The next day, we removed the inoculum, rinsed the cell monolayer with 1× phosphate-buffered saline (PBS), and added 25 ml of fresh DMEM containing 2% FBS. Two days later, when the cytopathic effect of the virus was clearly visible, as evidenced by a large number of round floating cells, we collected the culture medium, passed it through a 0.2- μ m filter, and stored it at -80°C. We then prepared the P2 working stock of the virus by infecting Vero E6 cells with the P1 stock at an MOI of 0.1 PFU/cell and harvesting the culture medium 3 days later.

To determine the titer of our viral stock by plaque assay, we seeded Vero E6 cells into a 12-well plate at a density of 2.5×10^5 cells per well. The next day, the cells were infected with serial 10-fold dilutions of the virus stock for 1 h at 37°C. We then added 1 ml per well of the overlay medium containing 2× DMEM (number 12800017; Gibco) supplemented with 4% FBS and mixed at a 1:1 ratio with 1.2% Avicel (RC-581; DuPont) to obtain the final concentrations of 2% and 0.6% for FBS and Avicel, respectively. Three days later, the overlay medium was removed, and the cell monolayer was washed with 1× PBS and fixed for 30 min at room temperature with 4% paraformaldehyde. Fixed cells were then washed with 1× PBS and stained for 1 h at room temperature with 0.1% crystal violet prepared in 10% ethanol-water. After rinsing with tap water, the number of plaques was counted and the virus titer was calculated. The titer of our P2 virus stock was 1×10^7 PFU/ml.

RT-qPCR. To measure the mRNA abundance of ISGs, total RNA was isolated from cells using a Qiagen RNeasy plus minikit (number 74134; Qiagen) according to the manufacturer's instructions, with an additional on-column DNase treatment (number 79256; Qiagen). RT-qPCR was performed using a Luna universal one-step RT-qPCR kit (number E3005L; New England Biolabs). Briefly, 12 μ l of reaction mixture containing 2 μ l of RNA, 0.4 μ M each forward and reverse primer, 0.6 μ l of the 20× Luna WarmStart RT enzyme mix, and 6 μ l of the 2× Luna universal one-step reaction mix was subjected to one-step RT-qPCR using Applied Biosystems QuantStudio 3 (ThermoFisher Scientific), with the following cycling conditions: reverse transcription at 50°C for 10 min, initial denaturation at 95°C for 2 min followed by 40 cycles of denaturation at 95°C for 15 s and annealing/extension at 60°C for 1 min, ending with melt curve analysis of the PCR product from 65°C to 95°C, rising in 0.5°C per s increments, waiting for 30 s at 65°C and for 5 s at each step thereafter, and acquiring fluorescence at each temperature increment. The threshold cycle (C_T) values were determined using the QuantStudio Design and Analysis software V1.5.1. RPS11 was used as a housekeeping gene, and the ISG C_T values were normalized against this gene to calculate the fold change between untreated and IFN-treated cells.

Immunofluorescence. Virus-infected cells were fixed in 4% paraformaldehyde for 30 min. The fixative was removed and the cell monolayer washed twice with 1× PBS. The cells were then permeabilized and incubated overnight at 4°C with anti-SARS-CoV nucleocapsid antibody (1:2,000 dilution). The cells were then washed 5 times with 1× PBS and stained with Alexa Fluor 568-conjugated goat anti-rabbit secondary antibody (1:1,000 dilution) (number A11008; Invitrogen) in the dark at room temperature for 1 h and counterstained with 4',6-diamidino-2-phenylindole (DAPI). Images were captured using an EVOS M5000 imaging system (ThermoFisher Scientific). For quantitative analysis of the fixed cell images, we used the MuviCyte live-cell imaging system (PerkinElmer, Waltham, MA). We acquired images of multiple microscopic fields per well using a 10× lens objective and counted the number of DAPI- and viral antigen-positive cells. For each of those images, we then calculated the percentage of DAPI-positive cells expressing the viral antigen and plotted the mean \pm standard deviation (SD) of multiple images for each condition.

Flow cytometry. For cell surface analysis of ACE2, we harvested cells and washed them in fluorescence-activated cell sorting (FACS) buffer (2% FBS in 1× PBS). Cells were resuspended in a 1:50 dilution of human F_c blocking solution (number 422302; BioLegend) and incubated on ice for 10 min. Human ACE2 antibody or goat IgG isotype control was then added to the cells to obtain the final concentration of 5 μ g/ml followed by 1 h of incubation on ice. The cells were washed with FACS buffer and incubated for 30 min on ice in the dark with a 1:400 dilution of Alexa Fluor 488 donkey anti-goat secondary antibody (number A11055; Invitrogen). The cells were washed and resuspended in FACS buffer. Data were collected using a BD LSR II flow cytometer and analyzed with FlowJo software (version 10).

Sample preparation for proteomic analysis. We infected cells grown to a confluence of 90 to 95% in 6-well plates with SARS-CoV-2 at an MOI of 1. To synchronize virus entry into cells, the infection was

carried out in a small volume of Opti-MEM (400 μ l per well) on ice for 1 h, followed by removal of the virus inoculum, addition of 2 ml of DMEM containing 2% FBS, and incubation at 37°C. To harvest cells, the culture medium was removed and the cell monolayer was washed twice with 1 \times PBS, followed by cell scraping in a lysis buffer comprising 6 M GuHCl, 100 mM Tris, pH 8.0, 40 mM chloroacetamide, and 10 mM Tris(2-carboxyethyl)phosphine hydrochloride (TCEP), supplemented with Complete Mini protease (number 11836170001; Roche) and phosphatase inhibitor cocktails (number 04906837001; Roche). Lysates were boiled at 100°C for 15 min and sonicated briefly. Total proteins were quantified via Bradford assay and normalized prior to digestion with trypsin (Pierce) at a 1:50 ratio (enzyme to protein, wt/wt) overnight at 37°C. Digestion was quenched with trifluoroacetic acid, and the peptides were desalted using Sep-Pak C₁₈ columns (WAT054955; Waters Corporation). Desalted peptides were labeled with tandem mass tags (TMT) using TMTPro-16plex isobaric tags (number A44520; ThermoFisher Scientific) per the manufacturer's instructions. Replicate samples corresponding to each time point for each cell line were labeled separately. The TMT-labeled peptides for the respective cell lines were then pooled, desalted, and fractionated via basic reversed-phase fractionation using a mobile phase comprising 0.1% NH₄OH and various acetonitrile concentrations (5%, 10%, 12.5%, 15%, 17.5%, 20%, 22.5%, 25%, 30%, 35%, 40%, and 60%). For each cell line, two early (5% and 10%) fractions were orthogonally concatenated with two late (40% and 60%) fractions, resulting in total of 10 fractions per cell line for analyses. All fractions were dried in a SpeedVac vacuum concentrator (ThermoFisher Scientific).

Mass spectrometry analysis. Dried samples were reconstituted in mobile phase A solvent (2% acetonitrile and 0.1% formic acid) for analysis on the Q-Exactive HF-X mass spectrometer (ThermoFisher Scientific), interfaced to the Easy NanoLC1200 high-performance liquid chromatography system (ThermoFisher Scientific). The peptides were loaded on a reversed-phase Nanotrap column in mobile phase A (75- μ m inner diameter by 2 cm; Acclaim PepMap100 C₁₈ 3 μ m; 100 Å; number 164946; ThermoFisher Scientific) and separated over an EASY-Spray column, (number ES803A; ThermoFisher Scientific) using a gradient (6% to 19% over 58 min and then 19% to 36% over 34 min) of mobile phase B (0.1% formic acid, 80% acetonitrile) at a flow rate of 250 nl/min. The mass spectrometer was operated in positive ion mode with a spray voltage of 2,100 V, and the data were acquired in data-dependent acquisition (DDA) mode. Precursor scans were acquired at a resolution of 120,000 full width at half maximum (FWHM), with a maximum injection time of 120 ms. The top 12 most abundant ions, with charge states of ≥ 2 , were selected for fragmentation by high-energy collisional dissociation (HCD; collision energy, 29%) and analyzed at a resolution of 45,000 FWHM with a maximum injection time of 250 ms.

Analysis of raw mass spectrometry data. All raw data were processed using MaxQuant (version 1.6.7.0). The acquired tandem spectra were searched against the reference *Homo sapiens* proteome (taxonomic ID 9606) FASTA file downloaded from UniProt in April 2017, concatenated with common contaminants and SARS-CoV-2 proteome sequences. TMT reporter ion quantification was performed on MaxQuant using default settings. For searches, cysteine carbamidomethylation was specified as fixed modification, and oxidation of methionine and N-terminal protein acetylation were set as variable modifications. Enzyme specificity was set to trypsin, and up to two missed cleavages were allowed. The MaxQuant output file, designated "ProteinGroups.txt," was used for data normalization and statistical analyses using in-house-generated scripts in the R environment.

Data analysis and pathway enrichment. Bioinformatic analysis was performed using R (R Foundation for Statistical Computing, Vienna, Austria; <http://www.R-project.org>), version 3.6.1. The ProteinGroups.txt table corresponding to each cell line was filtered to eliminate entries labeled as reverse hits, potential contaminants, and "only identified by site." Protein quantitation required at least 70% valid values across all TMT channels. The TMT intensity values were log₂ transformed and Loess normalized. Differentially regulated proteins were defined by implementing a log₂ fold change threshold of 0.25 for SARS-CoV-2 versus mock-infected cells. Similar liberal thresholds have been previously described for TMT-based analyses owing to ratio compression (60). For functional enrichment of proteins based on clustering between the respective time points, Enrichr was used with the Reactome database of pathways. For differential analysis, the LIMMA (61) R package was used to fit a linear model accounting for the infection versus mock condition at each time point. Moderated *t* tests were corrected with the Benjamini-Hochberg method for false discovery rate (FDR). Gene set enrichment analysis was performed using the fgsea R package (<https://www.biorxiv.org/content/early/2016/06/20/060012>) using curated gene library (62) ranked lists, where the gene rank is defined as $-\log(P \text{ value}) \times \text{sign}(\log_2 \text{ fold change})$ (63). In the case of duplicate proteins mapping to a common gene symbol, the one with the highest absolute value rank was retained.

Differentiation of hiPSC into cardiomyocytes. hiPSCs from the PGP1 parent line (GM23338; Coriell Institute), engineered to have an endogenous green fluorescent protein tag on one titin allele (64), were provided by the Seidman Lab. hiPSCs were seeded into tissue culture-treated plates coated with Matrigel (number CB-40230; ThermoFisher Scientific) mixed 1:80 in DMEM/F-12 (number 11330-057; ThermoFisher Scientific), maintained in mTeSR1 (number 85870; StemCell), and passaged using Accutase (number A6964; Sigma) at 60 to 90% confluence. hiPSCs were differentiated into cardiomyocytes (hiPSC-CMs) by small-molecule, monolayer-based manipulation of the Wnt-signaling pathway. Briefly, the cells were grown from day 0 to day 9 in RPMI 1640/GlutaMAX medium (number 61870036; ThermoFisher Scientific) containing the insulin-free B-27 supplement (number A1895601; ThermoFisher Scientific). On day 0, the cells were treated with 12 μ M CHIR99021 (number 4423; Tocris) for 24 h to activate WNT signaling. Two days later (on day 3), 5 μ M IWP4 (number 5214; Tocris) was added to the culture medium for 48 h to block the WNT signaling. On day 9, the culture medium was replaced with RPMI 1640/GlutaMAX medium supplemented with insulin-containing B-27 supplement (number 17504-044; ThermoFisher Scientific). On day 11, metabolic selection of hiPSC-CMs was started by growing them in a

glucose-free RPMI 1640 medium (number 11879020; ThermoFisher Scientific) containing 4 mM sodium D,L-lactate solution (number L426; Sigma) for 4 days, replenishing the medium every 2 days.

Following metabolic selection, purified hiPSC-CMs were trypsinized with 0.25% trypsin-EDTA (number 25200114; ThermoFisher Scientific) containing 10 μ g/ml DNase I (number 7469; StemCell) and replated into 12-well plates coated with 10 μ g/ml human bulk fibronectin (number 3560; ThermoFisher Scientific) at a density of 750,000 cells/well. The replating medium comprised RPMI 1640 mixed with the insulin-containing B-27 supplement, 2% fetal bovine serum (number F0926; Sigma), and 5 μ M Y-2763 (number 12543; Tocris). The cells were maintained in RPMI 1640 medium supplemented with insulin-containing B-27 until days 30 to 50, with the medium being replenished every 2 days. For SARS-CoV-2 infection, hiPSC-CMs were seeded into either 96- or 12-well plates coated with 10 μ g/ml fibronectin.

Interferon response assays. To test interferon response in uninfected and SARS-CoV-2-infected cells, we seeded cells either in 6-well plates (for Western blotting) at a density of 5×10^5 cells per well, in 12-well plates at a density of 2×10^5 cells per well (for RT-qPCR), or in 96-well plates at a density of 2.5×10^4 cells per well (for IF). The next day, the cells were infected with SARS-CoV-2 at an MOI of 1 or left uninfected. Twenty-four hours later, we treated the cells with different concentrations of IFN- α for 15 to 30 min (for Western blotting and IF) or for 1, 2, 4, and 8 h (for RT-qPCR). The cells were then processed for downstream applications.

Ubiquitination assay. To examine ubiquitination of ectopically expressed IFNAR1, 293T cells expressing ACE2/TMPRSS2 were transfected with FLAG-IFNAR1 and HA-ubiquitin for 36 h and then infected with SARS-CoV-2 for 12 h or treated with thapsigargin (2 μ M) for 30 min. The cells were lysed in 1% SDS followed by quenching of SDS with a 10-fold excess of Triton X-100. Five hundred micrograms of total protein was used for immunoprecipitation with anti-FLAG M2 agarose beads (number A2220; Sigma) at 4°C for 2 h, and IFNAR1 ubiquitination was assessed by Western blotting with an anti-HA antibody (number F7425; Sigma). To assess ubiquitination of endogenous IFNAR1, ACE2/TMPRSS2-expressing 293T cells were transfected with FLAG-tagged TR-TUBE for 36 h, followed by infection with SARS-CoV-2 for 12 h and as a positive control with VSV (MOI of 0.01) for 12 h. The cells were harvested in lysis buffer containing 0.25% NP-40, and 500 μ g of total protein was subjected to immunoprecipitation with anti-FLAG M2 agarose beads (Sigma) followed by detection of polyubiquitinated IFNAR1 by Western blotting with an anti-IFNAR1 antibody.

Western blotting. Proteins from various cells were extracted with 1 \times RIPA buffer containing 1 \times complete-mini protease inhibitor (number 11836170001; Roche) and 1 \times phosphatase inhibitor cocktail (number 04906837001; Roche). Samples were incubated on ice for 30 min and centrifuged at 12,000 \times g for 20 min at 4°C. The supernatants were transferred to new ice-cold Eppendorf tubes, and protein concentration was measured by the bicinchoninic acid (BCA) assay using the Pierce BCA protein assay kit (number 23225; ThermoFisher Scientific). Equal amounts of protein were loaded on 4 to 12% SDS-PAGE gel and transferred onto nitrocellulose membrane. Following staining with primary and secondary (Li-Cor) antibodies, the bands were visualized by scanning the membrane with the Li-Cor CLx infrared scanner. The intensity of protein bands was measured in the open-source package ImageJ.

Availability of raw data. The mass spectrometry proteomics data have been deposited in the ProteomeXchange Consortium (65) via the PRIDE (66) partner repository at <http://proteomecentral.proteomexchange.org/cgi/GetDataset?ID=PXD022027> and <https://www.ebi.ac.uk/pride/archive/projects/PXD022027>, respectively.

SUPPLEMENTAL MATERIAL

Supplemental material is available online only.

SUPPLEMENTAL FILE 1, XLSX file, 1.4 MB.

ACKNOWLEDGMENTS

We thank George J. Murphy (Boston University, Boston) for AC-16 cells, Thomas Gallagher (Loyola University, Maywood) for hACE2 and hTMPRSS2 expression plasmids, Shafi Kuchay (University of Illinois, Chicago) for Tr-TUBE expression plasmids, and Elke Muhlberger (Boston University, Boston) for reagents. We also thank William M. Schneider (The Rockefeller University) and Mikel Garcia-Marcos (Boston University) for critical reading of the manuscript.

This work was supported by Boston University startup funds (to M.S., F.D., and A.E.), Evergrande MassCPR awards (to M.S. and D.N.K.), Peter Paul Career Development Award (to F.D.), National Cancer Institute (NCI R01CA175382) and National Institutes of Health (NIH R01HL132325) (to V.C.C.), National Institutes of Health (NIH R01 AI085089) (to S.C.B.), National Science Foundation Graduate Research Fellowship (to J.K.E.), and National Science Foundation Nanosystems Engineering Research Center for Directed Multiscale Assembly of Cellular Metamaterials (to C.S.C.).

M.S. conceptualized the study. D.-Y.C., N.K., B.J.C., H.L.C., A.H.T., D.K., H.L.C., F.D., and M.S. performed the experiments. R.K.G. performed mass spectrometry analyses of SARS-CoV-2-infected cells. J.K.E. and C.S.C. provided hiPSC-CMs. B.B., R.K.G., and M.S.

performed data analysis, and N.A.C., V.C.C., D.N.K., S.C.B., S.Y.F., and J.H.C. provided reagents and scientific input. M.S., D.-Y.C., R.K.G., F.D., and A.E. interpreted the results. M.S. and J.H.C. wrote and revised the manuscript. All authors read and approved the manuscript.

REFERENCES

- Zhou P, Yang X-L, Wang X-G, Hu B, Zhang L, Zhang W, Si H-R, Zhu Y, Li B, Huang C-L, Chen H-D, Chen J, Luo Y, Guo H, Jiang R-D, Liu M-Q, Chen Y, Shen X-R, Wang X, Zheng X-S, Zhao K, Chen Q-J, Deng F, Liu L-L, Yan B, Zhan F-X, Wang Y-Y, Xiao G-F, Shi Z-L. 2020. A pneumonia outbreak associated with a new coronavirus of probable bat origin. *Nature* 579:270–273. <https://doi.org/10.1038/s41586-020-2012-7>.
- Borczuk AC, Salvatore SP, Seshan SV, Patel SS, Bussell JB, Mostyka M, Elsoukary S, He B, Del Vecchio C, Fortarezza F, Pezzuto F, Navalesi P, Crisanti A, Fowkes ME, Bryce CH, Calabrese F, Beasley MB. 2020. COVID-19 pulmonary pathology: a multi-institutional autopsy cohort from Italy and New York City. *Mod Pathol* 33:2156–2168. <https://doi.org/10.1038/s41379-020-00661-1>.
- Qian Q, Fan L, Liu W, Li J, Yue J, Wang M, et al. 2020. Direct evidence of active SARS-CoV-2 replication in the intestine. *Clin Infect Dis* <https://doi.org/10.1093/cid/ciaa925>.
- Lamers MM, Beumer J, van der Vaart J, Knoops K, Puschhof J, Breugem TI, Ravelli RBG, Paul van Schayck J, Mykytyn AZ, Duimel HQ, van Donselaar E, Riesebosch S, Kuijpers HJH, Schipper D, van de Wetering WJ, de Graaf M, Koopmans M, Cuppen E, Peters PJ, Haagmans BL, Clevers H. 2020. SARS-CoV-2 productively infects human gut enterocytes. *Science* 369:50–54. <https://doi.org/10.1126/science.abc1669>.
- Wang Y, Liu S, Liu H, Li W, Lin F, Jiang L, Li X, Xu P, Zhang L, Zhao L, Cao Y, Kang J, Yang J, Li L, Liu X, Li Y, Nie R, Mu J, Lu F, Zhao S, Lu J, Zhao J. 2020. SARS-CoV-2 infection of the liver directly contributes to hepatic impairment in patients with COVID-19. *J Hepatol* 73:807–816. <https://doi.org/10.1016/j.jhep.2020.05.002>.
- Zhao B, Ni C, Gao R, Wang Y, Yang L, Wei J, Lv T, Liang J, Zhang Q, Xu W, Xie Y, Wang X, Yuan Z, Liang J, Zhang R, Lin X. 2020. Recapitulation of SARS-CoV-2 infection and cholangiocyte damage with human liver ductal organoids. *Protein Cell* 11:771–775. <https://doi.org/10.1007/s13238-020-00718-6>.
- Puelles VG, Lütgehetmann M, Lindenmeyer MT, Sperhake JP, Wong MN, Allweiss L, Chilla S, Heinemann A, Wanner N, Liu S, Braun F, Lu S, Pfefferle S, Schröder AS, Edler C, Gross O, Glatzel M, Wichmann D, Wietz T, Kluge S, Püschel K, Aepfelbacher M, Huber TB. 2020. Multiorgan and renal tropism of SARS-CoV-2. *N Engl J Med* 383:590–592. <https://doi.org/10.1056/NEJMc2011400>.
- Monteil V, Kwon H, Prado P, Hagelkrüys A, Wimmer RA, Stahl M, Leopoldi A, Garreta E, Hurtado Del Pozo C, Prosper F, Romero JP, Wirnsberger G, Zhang H, Slutsky AS, Conder R, Montserrat N, Mirazimi A, Penninger JM. 2020. Inhibition of SARS-CoV-2 infections in engineered human tissues using clinical-grade soluble human ACE2. *Cell* 181:905–913. <https://doi.org/10.1016/j.cell.2020.04.004>.
- Sharma A, Garcia G, Wang Y, Plummer JT, Morizono K, Arumugaswami V, Svendsen CN. 2020. Human iPSC-derived cardiomyocytes are susceptible to SARS-CoV-2 infection. *Cell Rep Med* 1:100052. <https://doi.org/10.1016/j.xcrm.2020.100052>.
- Lindner D, Fitzek A, Bräuninger H, Aleshcheva G, Edler C, Meissner K, Scherschel K, Kirchhof P, Escher F, Schultheiss H-P, Blankenberg S, Püschel K, Westermann D. 2020. Association of cardiac infection With SARS-CoV-2 in confirmed COVID-19 autopsy cases. *JAMA Cardiol* 5:1281. <https://doi.org/10.1001/jamacardio.2020.3551>.
- Zhang B-Z, Chu H, Han S, Shuai H, Deng J, Hu Y-f, Gong H-r, Lee AC-Y, Zou Z, Yau T, Wu W, Hung IF-N, Chan JF-W, Yuen K-Y, Huang J-D. 2020. SARS-CoV-2 infects human neural progenitor cells and brain organoids. *Cell Res* 30:928–931. <https://doi.org/10.1038/s41422-020-0390-x>.
- Song E, Zhang C, Israelow B, Lu-Culligan A, Prado AV, Skriabine S, et al. 2021. Neuroinvasion of SARS-CoV-2 in human and mouse brain. *J Exp Med* 218. <https://doi.org/10.1084/jem.20202135>.
- Wei J, Alfajaro MM, DeWeirdt PC, Hanna RE, Lu-Culligan WJ, Cai WL, Strine MS, Zhang S-M, Graziano VR, Schmitz CO, Chen JS, Mankowski MC, Filler RB, Ravindra NG, Gasque V, de Miguel FJ, Patil A, Chen H, Oguntuyo KY, Abriola L, Surovtseva YV, Orchard RC, Lee B, Lindenbach BD, Politi K, van Dijk D, Kadoch C, Simon MD, Yan Q, Doench JG, Wilen CB. 2021. Genome-wide CRISPR screens reveal host factors critical for SARS-CoV-2 infection. *Cell* 184:76–91. <https://doi.org/10.1016/j.cell.2020.10.028>.
- Xia H, Cao Z, Xie X, Zhang X, Chen JY-C, Wang H, Menachery VD, Rajsbaum R, Shi P-Y. 2020. Evasion of type I interferon by SARS-CoV-2. *Cell Rep* 33:108234. <https://doi.org/10.1016/j.celrep.2020.108234>.
- Yuen C-K, Lam J-Y, Wong W-M, Mak L-F, Wang X, Chu H, Cai J-P, Jin D-Y, To KK-W, Chan JF-W, Yuen K-Y, Kok K-H. 2020. SARS-CoV-2 nsp13, nsp14, nsp15 and orf6 function as potent interferon antagonists. *Emerg Microbes Infect* 9:1418–1428. <https://doi.org/10.1080/22221751.2020.1780953>.
- Miorin L, Kehrer T, Sanchez-Aparicio MT, Zhang K, Cohen P, Patel RS, Cupic A, Makio T, Mei M, Moreno E, Danziger O, White KM, Rathnasinghe R, Uccellini M, Gao S, Aydillo T, Mena I, Yin X, Martin-Sancho L, Krogan NJ, Chanda SK, Schotsaert M, Wozniak RW, Ren Y, Rosenberg BR, Fountoura BMA, Garcia-Sastre A. 2020. SARS-CoV-2 Orf6 hijacks Nup98 to block STAT nuclear import and antagonize interferon signaling. *Proc Natl Acad Sci U S A* 117:28344–28354. <https://doi.org/10.1073/pnas.2016650117>.
- Karp NA, Huber W, Sadowski PG, Charles PD, Hester SV, Lilley KS. 2010. Addressing accuracy and precision issues in iTRAQ quantitation. *Mol Cell Proteomics* 9:1885–1897. <https://doi.org/10.1074/mcp.M900628-MCP200>.
- Bojkova D, Klann K, Koch B, Widera M, Krause D, Ciesek S, Cinatl J, Münch C. 2020. Proteomics of SARS-CoV-2-infected host cells reveals therapy targets. *Nature* 583:469–472. <https://doi.org/10.1038/s41586-020-2332-7>.
- Cathcart AL, Rozovics JM, Semler BL. 2013. Cellular mRNA decay protein AUF1 negatively regulates enterovirus and human rhinovirus infections. *J Virol* 87:10423–10434. <https://doi.org/10.1128/JVI.01049-13>.
- Bouhaddou M, Memon D, Meyer B, White KM, Rezelj VV, Correa Marrero M, Polacco BJ, Melnyk JE, Ulferts S, Kaake RM, Batra J, Richards AL, Stevenson E, Gordon DE, Rojc A, Obernier K, Fabius JM, Soucheray M, Miorin L, Moreno E, Koh C, Tran QD, Hardy A, Robinot R, Vallet T, Nilsson-Payant BE, Hernandez-Armenta C, Dunham A, Weigang S, Knerr J, Modak M, Quintero D, Zhou Y, Dugourd A, Valdeolivas A, Patil T, Li Q, Hüttenhain R, Cakir M, Muralidharan M, Kim M, Jang G, Tutuncuoglu B, Hiatt J, Guo JZ, Xu J, Bouhaddou S, Mathy CJ, Gaulton A, Manners EJ, et al. 2020. The global phosphorylation landscape of SARS-CoV-2 infection. *Cell* 182:685–712. <https://doi.org/10.1016/j.cell.2020.06.034>.
- Saeed M, Kapell S, Hertz NT, Wu X, Bell K, Ashbrook AW, Mark MT, Zebroski HA, Neal ML, Flodström-Tullberg M, MacDonald MR, Aitchison JD, Molina H, Rice CM. 2020. Defining the proteolytic landscape during enterovirus infection. *PLoS Pathog* 16:e1008927. <https://doi.org/10.1371/journal.ppat.1008927>.
- Hammaren HM, Virtanen AT, Raivola J, Silvennoinen O. 2019. The regulation of JAKs in cytokine signaling and its breakdown in disease. *Cytokine* 118:48–63. <https://doi.org/10.1016/j.cyto.2018.03.041>.
- Ghoreschi K, Laurence A, O'Shea JJ. 2009. Janus kinases in immune cell signaling. *Immunol Rev* 228:273–287. <https://doi.org/10.1111/j.1600-065X.2008.00754.x>.
- Horvath CM. 2004. The Jak-STAT pathway stimulated by interferon alpha or interferon beta. *Sci STKE* 2004:tr10–tr10. <https://doi.org/10.1126/stke.2602004tr10>.
- Mosca JD, Pitha PM. 1986. Transcriptional and posttranscriptional regulation of exogenous human beta interferon gene in simian cells defective in interferon synthesis. *Mol Cell Biol* 6:2279–2283. <https://doi.org/10.1128/MCB.6.6.2279>.
- Heinrich PC, Behrmann I, Haan S, Hermanns HM, Müller-Newen G, Schaper F. 2003. Principles of interleukin (IL)-6-type cytokine signalling and its regulation. *Biochem J* 374:1–20. <https://doi.org/10.1042/BJ20030407>.
- Bhattacharya S, Qian J, Tzimas C, Baker DP, Koumenis C, Diehl JA, Fuchs SY. 2011. Role of p38 protein kinase in the ligand-independent ubiquitination and down-regulation of the IFNAR1 chain of type I interferon receptor. *J Biol Chem* 286:22069–22076. <https://doi.org/10.1074/jbc.M111.238766>.
- Yoshida Y, Saeki Y, Murakami A, Kawawaki J, Tsuchiya H, Yoshihara H, Shindo M, Tanaka K. 2015. A comprehensive method for detecting ubiquitinated

- substrates using TR-TUBE. *Proc Natl Acad Sci U S A* 112:4630–4635. <https://doi.org/10.1073/pnas.1422313112>.
29. Kuchay S, Saeed M, Giorgi C, Li J, Hoffmann H-H, Pinton P, Rice CM, Pagano M. 2018. NS5A promotes constitutive degradation of IP3R3 to counteract apoptosis induced by hepatitis C virus. *Cell Rep* 25:833–840. <https://doi.org/10.1016/j.celrep.2018.09.088>.
 30. Febvre-James M, Lecureur V, Augagneur Y, Mayati A, Fardel O. 2018. Repression of interferon beta-regulated cytokines by the JAK1/2 inhibitor ruxolitinib in inflammatory human macrophages. *Int Immunopharmacol* 54:354–365. <https://doi.org/10.1016/j.intimp.2017.11.032>.
 31. Sanchez GAM, Reinhardt A, Ramsey S, Wittkowski H, Hashkes PJ, Berkun Y, Schalm S, Murias S, Dare JA, Brown D, Stone DL, Gao L, Klausmeier T, Foell D, de Jesus AA, Chapelle DC, Kim H, Dill S, Colbert RA, Failla L, Kost B, O'Brien M, Reynolds JC, Folio LR, Calvo KR, Paul SM, Weir N, Brofferio A, Soldato A, Biancotto A, Cowen EW, Digiovanna JJ, Gadina M, Lipton AJ, Hadigan C, Holland SM, Fontana J, Alawad AS, Brown RJ, Rother KI, Heller T, Brooks KM, Kumar P, Brooks SR, Waldman M, Singh HK, Nickeleit V, Silk M, Prakash A, Janes JM, et al. 2018. JAK1/2 inhibition with baricitinib in the treatment of autoinflammatory interferonopathies. *J Clin Invest* 128:3041–3052. <https://doi.org/10.1172/JCI98814>.
 32. Bastard P, Rosen LB, Zhang Q, Michailidis E, Hoffmann H-H, Zhang Y, Dorgham K, Philippot Q, Rosain J, Béziat V, Manry J, Shaw E, Haljasmägi L, Peterson P, Lorenzo L, Bizien L, Trouillet-Assant S, Dobbs K, de Jesus AA, Belot A, Kallaste A, Catherinot E, Tandjaoui-Lambiotte Y, Le Pen J, Kerner G, Bigio B, Seeleuthner Y, Yang R, Bolze A, Spaan AN, Delmonte OM, Abers MS, Aiuti A, Casari G, Lampasona V, Piemonti L, Ciceri F, Bilguvar K, Lifton RP, Vasse M, Smadja DM, Migaud M, Hadjadj J, Terrier B, Duffy D, Quintana-Murci L, van de Beek D, Roussel L, Gaudin S, Tangye SG, HGID Lab, et al. 2020. Auto-antibodies against type I IFNs in patients with life-threatening COVID-19. *Science* 370:eabd4585. <https://doi.org/10.1126/science.abd4585>.
 33. Zhang Q, Bastard P, Liu Z, Le Pen J, Moncada-Velez M, Chen J, Ogishi M, Sabli IKD, Hodeib S, Korol C, Rosain J, Bilguvar K, Ye J, Bolze A, Bigio B, Yang R, Arias AA, Zhou Q, Zhang Y, Onodi F, Korniotis S, Karpf L, Philippot Q, Chbihi M, Bonnet-Madin L, Dorgham K, Smith N, Schneider WM, Razoogy BS, Hoffmann H-H, Michailidis E, Moens L, Han JE, Lorenzo L, Bizien L, Meade P, Neehus A-L, Ugurbil AC, Corneau A, Kerner G, Zhang P, Rapaport F, Seeleuthner Y, Manry J, Masson C, Schmitt Y, Schlüter A, Le Voyer T, Khan T, Li J, COVID-STORM Clinicians, et al. 2020. Inborn errors of type I IFN immunity in patients with life-threatening COVID-19. *Science* 370:eabd4570. <https://doi.org/10.1126/science.abd4570>.
 34. Matsumiya T, Stafforini DM. 2010. Function and regulation of retinoic acid-inducible gene-1. *Crit Rev Immunol* 30:489–513. <https://doi.org/10.1615/critrevimmunol.v30.i6.10>.
 35. Honda K, Yanai H, Negishi H, Asagiri M, Sato M, Mizutani T, Shimada N, Ohba Y, Takaoka A, Yoshida N, Taniguchi T. 2005. IRF-7 is the master regulator of type-I interferon-dependent immune responses. *Nature* 434:772–777. <https://doi.org/10.1038/nature03464>.
 36. Marie I, Durbin JE, Levy DE. 1998. Differential viral induction of distinct interferon-alpha genes by positive feedback through interferon regulatory factor-7. *EMBO J* 17:6660–6669. <https://doi.org/10.1093/emboj/17.22.6660>.
 37. Lee CK, Bluysen HA, Levy DE. 1997. Regulation of interferon-alpha responsiveness by the duration of Janus kinase activity. *J Biol Chem* 272:21872–21877. <https://doi.org/10.1074/jbc.272.35.21872>.
 38. Colamonici O, Yan H, Domanski P, Handa R, Smalley D, Mullersman J, Witte M, Krishnan K, Krolewski J. 1994. Direct binding to and tyrosine phosphorylation of the alpha subunit of the type I interferon receptor by p135tyk2 tyrosine kinase. *Mol Cell Biol* 14:8133–8142. <https://doi.org/10.1128/mcb.14.12.8133-8142.1994>.
 39. Larner AC, Chaudhuri A, Darnell JE, Jr. 1986. Transcriptional induction by interferon. New protein(s) determine the extent and length of the induction. *J Biol Chem* 261:453–459. [https://doi.org/10.1016/S0021-9258\(17\)42492-6](https://doi.org/10.1016/S0021-9258(17)42492-6).
 40. Hoffmann M, Kleine-Weber H, Schroeder S, Krüger N, Herrler T, Erichsen S, Schiergens TS, Herrler G, Wu N-H, Nitsche A, Müller MA, Drosten C, Pöhlmann S. 2020. SARS-CoV-2 cell entry depends on ACE2 and TMPRSS2 and is blocked by a clinically proven protease inhibitor. *Cell* 181:271–280. <https://doi.org/10.1016/j.cell.2020.02.052>.
 41. Steuten K, Kim H, Widen JC, Babin BM, Onguka O, Lovell S, et al. 2021. Challenges for targeting SARS-CoV-2 proteases as a therapeutic strategy for COVID-19. *ACS Infect Dis* <https://doi.org/10.1021/acinfecdis.0c00815>.
 42. Stanifer ML, Kee C, Cortese M, Zumaran CM, Triana S, Mukenhirn M, Kraeusslich H-G, Alexandrov T, Bartenschlager R, Boulant S. 2020. Critical role of type III interferon in controlling SARS-CoV-2 infection in human intestinal epithelial cells. *Cell Rep* 32:107863. <https://doi.org/10.1016/j.celrep.2020.107863>.
 43. Mantlo E, Bukreyeva N, Maruyama J, Paessler S, Huang C. 2020. Antiviral activities of type I interferons to SARS-CoV-2 infection. *Antiviral Res* 179:104811. <https://doi.org/10.1016/j.antiviral.2020.104811>.
 44. Rebendenne A, Chaves Valadão AL, Tauziat M, Maarifi G, Bonaventure B, McKellar J, Planès R, Nisole S, Arnaud-Arnould M, Moncorgé O, Goujon C. 2021. SARS-CoV-2 triggers an MDA-5-dependent interferon response which is unable to control replication in lung epithelial cells. *J Virol* 95:e02415-20. <https://doi.org/10.1128/JVI.02415-20>.
 45. Wang N, Zhan Y, Zhu L, Hou Z, Liu F, Song P, Qiu F, Wang X, Zou X, Wan D, Qian X, Wang S, Guo Y, Yu H, Cui M, Tong G, Xu Y, Zheng Z, Lu Y, Hong P. 2020. Retrospective multicenter cohort study shows early interferon therapy is associated with favorable clinical responses in COVID-19 patients. *Cell Host Microbe* 28:455–464. <https://doi.org/10.1016/j.chom.2020.07.005>.
 46. Channappanavar R, Fehr AR, Zheng J, Wohlford-Lenane C, Abrahante JE, Mack M, Sompallae R, McCray PB, Meyerholz DK, Perlman S. 2019. IFN-I response timing relative to virus replication determines MERS coronavirus infection outcomes. *J Clin Invest* 129:3625–3639. <https://doi.org/10.1172/JCI126363>.
 47. Lee C, Lim HK, Sakong J, Lee YS, Kim JR, Baek SH. 2006. Janus kinase-signal transducer and activator of transcription mediates phosphatidic acid-induced interleukin (IL)-1beta and IL-6 production. *Mol Pharmacol* 69:1041–1047. <https://doi.org/10.1124/mol.105.018481>.
 48. Jain A, Pasare C. 2017. Innate control of adaptive immunity: beyond the three-signal paradigm. *J Immunol* 198:3791–3800. <https://doi.org/10.4049/jimmunol.1602000>.
 49. Rao VUS, Arakeri G, Subash A, Rao J, Jadhav S, Suhail Sayeed M, Rao G, Brennan PA. 2020. COVID-19: loss of bridging between innate and adaptive immunity? *Med Hypotheses* 144:109861. <https://doi.org/10.1016/j.mehy.2020.109861>.
 50. Du SQ, Yuan W. 2020. Mathematical modeling of interaction between innate and adaptive immune responses in COVID-19 and implications for viral pathogenesis. *J Med Virol* 92:1615–1628. <https://doi.org/10.1002/jmv.25866>.
 51. Hadjadj J, Yatim N, Barnabei N, Corneau A, Boussier J, Smith N, Péré H, Charbit B, Bonnet V, Chenevier-Gobeaux C, Breillat P, Carlier N, Gaultier R, Morbieu C, Pène F, Marin N, Roche N, Szwedebel T-A, Merklings SH, Treluyer J-M, Veyer D, Mouthon L, Blanc C, Tharaux P-L, Rozenberg F, Fischer A, Duffy D, Rieux-Laucat F, Kernéis S, Terrier B. 2020. Impaired type I interferon activity and inflammatory responses in severe COVID-19 patients. *Science* 369:718–724. <https://doi.org/10.1126/science.abc6027>.
 52. Stukalov A, Girault V, Grass V, Karayel O, Bergant V, Urban C, Haas DA, Huang Y, Oubraham L, Wang A, Hamad MS, Piras A, Hansen FM, Tanzer MC, Paron I, Zinzula L, Engleitner T, Reinecke M, Lavacca TM, Ehmann R, Wölfel R, Jores J, Kuster B, Protzer U, Rad R, Ziebuhr J, Thiel V, Scaturro P, Mann M, Pichlmair A. 2021. Multilevel proteomics reveals host perturbations by SARS-CoV-2 and SARS-CoV. *Nature* 594:246–252. <https://doi.org/10.1038/s41586-021-03493-4>.
 53. Kalil AC, Patterson TF, Mehta AK, Tomashek KM, Wolfe CR, Ghazaryan V, Marconi VC, Ruiz-Palacios GM, Hsieh L, Kline S, Tapson V, Iovine NM, Jain MK, Sweeney DA, El Sahly HM, Branche AR, Regalado Pineda J, Lye DC, Sandkovsky U, Luetskemeyer AF, Cohen SH, Finberg RW, Jackson PEH, Taiwo B, Paules CI, Arguinchoa H, Erdmann N, Ahuja N, Frank M, Oh M-D, Kim E-S, Tan SY, Mularski RA, Nielsen H, Ponce PO, Taylor BS, Larson LAnn, Roupheal NG, Saklawi Y, Cantos VD, Ko ER, Engemann JJ, Amin AN, Watanabe M, Billings J, Elie M-C, Davey RT, Burgess TH, Ferreira J, Green M, ACTT-2 Study Group Members, et al. 2021. Baricitinib plus remdesivir for hospitalized adults with Covid-19. *N Engl J Med* 384:795–807. <https://doi.org/10.1056/NEJMoa2031994>.
 54. Shang J, Wan Y, Luo C, Ye G, Gong Q, Auerbach A, Li F. 2020. Cell entry mechanisms of SARS-CoV-2. *Proc Natl Acad Sci U S A* 117:11727–11734. <https://doi.org/10.1073/pnas.2003138117>.
 55. Danilowski Z, Guo X, Sanjana NE. 2020. The D614G mutation in SARS-CoV-2 Spike increases transduction of multiple human cell types. *bioRxiv* <https://doi.org/10.1101/2020.06.14.151357>.
 56. Sun S-H, Chen Q, Gu H-J, Yang G, Wang Y-X, Huang X-Y, Liu S-S, Zhang N-N, Li X-F, Xiong R, Guo Y, Deng Y-Q, Huang W-J, Liu Q, Liu Q-M, Shen Y-L, Zhou Y, Yang X, Zhao T-Y, Fan C-F, Zhou Y-S, Qin C-F, Wang Y-C. 2020. A mouse model of SARS-CoV-2 infection and pathogenesis. *Cell Host Microbe* 28:124–133. <https://doi.org/10.1016/j.chom.2020.05.020>.
 57. Munoz-Fontela C, Dowling WE, Funnell SGP, Gsell PS, Riveros-Balta AX, Albrecht RA, et al. 2020. Animal models for COVID-19. *Nature* 586:509–515. <https://doi.org/10.1038/s41586-020-2787-6>.

58. Sandberg R, Ernberg I. 2005. Assessment of tumor characteristic gene expression in cell lines using a tissue similarity index (TSI). *Proc Natl Acad Sci U S A* 102:2052–2057. <https://doi.org/10.1073/pnas.0408105102>.
59. Zannis VI, Kurnit DM, Breslow JL. 1982. Hepatic apo-A-I and apo-E and intestinal apo-A-I are synthesized in precursor isoprotein forms by organ cultures of human fetal tissues. *J Biol Chem* 257:536–544. [https://doi.org/10.1016/S0021-9258\(19\)68397-3](https://doi.org/10.1016/S0021-9258(19)68397-3).
60. Shen B, Yi X, Sun Y, Bi X, Du J, Zhang C, Quan S, Zhang F, Sun R, Qian L, Ge W, Liu W, Liang S, Chen H, Zhang Y, Li J, Xu J, He Z, Chen B, Wang J, Yan H, Zheng Y, Wang D, Zhu J, Kong Z, Kang Z, Liang X, Ding X, Ruan G, Xiang N, Cai X, Gao H, Li L, Li S, Xiao Q, Lu T, Zhu Y, Liu H, Chen H, Guo T. 2020. Proteomic and metabolomic characterization of COVID-19 patient sera. *Cell* 182:59–72. <https://doi.org/10.1016/j.cell.2020.05.032>.
61. Ritchie ME, Phipson B, Wu D, Hu Y, Law CW, Shi W, Smyth GK. 2015. limma powers differential expression analyses for RNA-sequencing and microarray studies. *Nucleic Acids Res* 43:e47. <https://doi.org/10.1093/nar/gkv007>.
62. Merico D, Isserlin R, Stueker O, Emili A, Bader GD. 2010. Enrichment map: a network-based method for gene-set enrichment visualization and interpretation. *PLoS One* 5:e13984. <https://doi.org/10.1371/journal.pone.0013984>.
63. Reimand J, Isserlin R, Voisin V, Kucera M, Tannus-Lopes C, Rostamianfar A, Wadi L, Meyer M, Wong J, Xu C, Merico D, Bader GD. 2019. Pathway enrichment analysis and visualization of omics data using g:Profiler, GSEA, Cytoscape and EnrichmentMap. *Nat Protoc* 14:482–517. <https://doi.org/10.1038/s41596-018-0103-9>.
64. Sharma A, Toepfer CN, Ward T, Wasson L, Agarwal R, Conner DA, et al. 2018. CRISPR/Cas9-mediated fluorescent tagging of endogenous proteins in human pluripotent stem cells. *Curr Protoc Hum Genet* 96:21.11.1–21.11.20. <https://doi.org/10.1002/cphg.52>.
65. Deutsch EW, Bandeira N, Sharma V, Perez-Riverol Y, Carver JJ, Kundu DJ, García-Seisdedos D, Jarnuczak AF, Hewapathirana S, Pullman BS, Wertz J, Sun Z, Kawano S, Okuda S, Watanabe Y, Hermjakob H, MacLean B, MacCoss MJ, Zhu Y, Ishihama Y, Vizcaino JA. 2020. The ProteomeXchange consortium in 2020: enabling “big data” approaches in proteomics. *Nucleic Acids Res* 48:D1145–D1152. <https://doi.org/10.1093/nar/gkz984>.
66. Perez-Riverol Y, Csordas A, Bai J, Bernal-Llinares M, Hewapathirana S, Kundu DJ, Inuganti A, Griss J, Mayer G, Eisenacher M, Pérez E, Uszkoreit J, Pfeuffer J, Sachsenberg T, Yilmaz S, Tiwary S, Cox J, Audain E, Walzer M, Jarnuczak AF, Ternent T, Brazma A, Vizcaino JA. 2019. The PRIDE database and related tools and resources in 2019: improving support for quantification data. *Nucleic Acids Res* 47:D442–D450. <https://doi.org/10.1093/nar/gky1106>.